

1 **Estimation of Global Scale Carbon Fluxes Using Maximum Likelihood Ensemble Filter**

2 **K. M. P. Perera^{1*}, R. S. Lokupitiya¹, A. S. Denning², P. K. Patra³, D. Zupanski⁴, M.**
 3 **Zupanski⁵, R. G. N. Meegama⁶, E. Y. K. Lokupitiya⁷, I. Baker², D. Baker⁵, T. Machida⁸,**
 4 **H. Matsueda⁹, Y. Sawa^{9,10}, Y. Niwa⁸**

5 ¹Department of Statistics, University of Sri Jayewardenepura, Sri Lanka. ²Department of
 6 Atmospheric Science, Colorado State University, Fort Collins, Colorado, USA. ³Research
 7 Institute for Global Change, JAMSTEC, Yokohama, 236-0001, Japan. ⁴Zupanski Consulting,
 8 LLC, Fort Collins, CO, USA. ⁵Cooperative Institute for Research in the Atmosphere, Colorado
 9 State University, Fort Collins, CO, USA. ⁶Department of Computer Science, University of Sri
 10 Jayewardenepura, Sri Lanka. ⁷Department of Zoology and Environment Sciences, University
 11 of Colombo, Sri Lanka. ⁸Center for Global Environmental Research (CGER), National Institute
 12 for Environmental Studies (NIES), Japan. ⁹Oceanography and Geochemistry Research
 13 Department, Meteorological Research Institute, Tsukuba, Japan. ¹⁰Global Environment and
 14 Marine Department, Japan Meteorological Agency
 15

16 Manjula Perera (manjula@sjp.ac.lk)

17 **Key Points:**

- 18 • Densely observed regions showed comparable results with CarbonTracker (CT2017)
 19 and other similar studies.
 20 • MLEF seems to perform well with high dimensional CO₂ observation vectors such as
 21 satellite and aircraft measurements.
 22 • CO₂ fluxes were poorly recovered in the regions having few measurement sites.

23

24

25

26 Abstract

27 Inverse modelling method named Maximum likelihood Ensemble Filter (MLEF) was used to
28 estimate gridded surface CO₂ fluxes using continuous, flask and Comprehensive Observation
29 Network for TRace gases by AirLiner (CONTRAIL) data for the years 2009-2011. Here,
30 MLEF coupled with Parametric Chemistry Transport Model (PCTM) driven by Modern-Era
31 Retrospective analysis for Research and Applications, Version 2 (MERRA2) weather data has
32 been used. Flux estimation was done by solving separate multiplicative biases for
33 photosynthesis, respiration, and air-sea gas exchange fluxes. Hourly land fluxes derived from
34 Simple Biosphere-version 3 (SiB3) model, Takahashi ocean fluxes and Brenkert fossil fuel
35 emissions were used as the prior fluxes. The inversion was carried out by assimilating hourly
36 CO₂ observations, According to this study, North America showed about 60-80% uncertainty
37 reduction while the Asian and European regions showed moderate results with 50-60%
38 uncertainty reduction. Most other land and oceanic regions showed less than 30% uncertainty
39 reduction. The results were mainly compared with well-known CarbonTracker and some
40 parallel inversion studies by considering long-term averages of the estimated fluxes for the
41 TransCom regions. Boreal North America, Temperate North America and Australia showed
42 similar annual averages in each case. Tropical Asia and Europe showed comparable results
43 with all other studies except for the CarbonTracker. The biases were poorly constrained in the
44 regions having few measurement sites like South America, Africa and Eurasian Temperate
45 which showed completely different result with other studies.
46

47 1 Introduction

48 Carbon is an essential component for all life on earth and atmospheric carbon exists mainly as
49 the carbon dioxide (CO₂) gas. It is the single largest contributor to the global warming among
50 well-mixed greenhouse gases. The rapid increasing patterns in atmospheric CO₂ concentration
51 may lead to significant global climatic changes in the coming years. CO₂ concentration in the
52 atmosphere has shown a significant increase by 30% since 1950 (Al-Ghussain, 2018) which is
53 mainly due to the increasing human activities after industrial revolution. According to Le Quere
54 et al. (2018), fossil fuel combustion, cement production and gas flaring are the main sources of
55 CO₂. In order to make policy decisions on CO₂ emissions, there are several gatherings and
56 agreements among different countries and they need the knowledge of regional and country
57 level carbon fluxes to make policies on carbon emission. As a result, research on global carbon
58 cycle using different approaches to identify the spatiotemporal distribution of carbon sources
59 and sinks has become popular topic among researchers in the field.
60

61 Top-down atmospheric inversions and bottom-up biosphere models are the two main
62 fundamentally different approaches used in estimating carbon fluxes. Bottom-up biosphere
63 models typically simulate the atmosphere-terrestrial biosphere exchange based on the
64 understanding of complex exchange processes such as photosynthesis, respiration,
65 decomposition, land-use change emissions, fire emissions, etc. Another approach to estimate
66 biospheric CO₂ fluxes is the “top-down” estimation technique which uses the inverse modelling
67 method. This method estimate net CO₂ flux by the assimilating atmospheric CO₂ measurements
68 from global network using a transport model, with the prior information such as net land flux,
69 net ocean flux, fire emissions, and fossil fuel emissions. In literature, many studies were carried
70 out to infer regional sources and sinks by using inverse methods (Baker et al., 2006; Basu et
71 al., 2014; Bruhwiler et al., 2005; Gurney et al., 2002; Jiang et al., 2013; Kim et al., 2014; Kim
72 et al., 2017; Lokupitiya et al., 2008; Michalak et al., 2004; Patra et al., 2012; Peters et al., 2005;
73 Peylin et al., 2013; Piao, et al., 2009, 2013; Rödenbeck et al., 2003; Saeki et al., 2013; Tans et

74 al., 1990). But still they need more advanced knowledge on statistics and mathematics while
75 obtaining the accurate estimates.

76

77 Many researchers have discussed the advantages and disadvantages in both methods.
78 According to Chatterjee et al. (2012), in top-down approach the estimated fluxes are mainly
79 based on atmospheric CO₂ concentrations and it does not get the knowledge on biogeochemical
80 processes associated with the carbon cycle as it is possible by the bottom-up approaches. And
81 this may be a disadvantage of the method. Kondo et al. (2019) has highlighted potential
82 difficulties faced by CO₂ budget assessment methods based on above two approaches and
83 suggested several ways to obtain more robust estimates. According to the used top-down
84 atmospheric inverse models and biosphere models in their study, it was found that there were
85 no optimal combination of models of atmospheric inversions and biosphere models that are
86 capable of producing consistent budget estimates for all global regions. They have identified
87 that one reason for this variability is as the possibility of some modelling issues such as
88 differences in prior fluxes, model resolution, size of the control vector, data assimilation
89 window length, the rate of transporting CO₂ concentrations from a source region to
90 neighbouring regions through atmospheric transport model and the transport model errors.
91 Other than above reasons, variations in the measurement error covariance matrix and the prior
92 flux and its error covariance matrix also affect considerable differences in CO₂ flux
93 measurements (Sajeev et al., 2019). According to Kondo et al. (2019), the next main reason is
94 the dipole effect in the design of inversion systems. It was also mentioned in their study that
95 the poor representation of some processes such as forest regrowth, crop land harvesting and
96 management, wood harvesting and degradation in the biosphere models may greatly affect the
97 regional budget estimates while using the bottom-up approach.

98

99 Earlier, atmospheric CO₂ measurements are mainly collected by in-situ measurement sites,
100 ships and aircrafts. Top-down inverse modelling based on Bayesian synthesis or batch mode
101 inversion is the most commonly used approach to estimate CO₂ sources and sinks. However,
102 limited number of CO₂ measurements makes the inverse problem both under-determined and
103 ill-posed (Chatterjee, 2012). Although, the large region inversions were developed (Gurney et
104 al., 2002) to over-come this problem, it may lead to aggregation errors (Kaminski et al., 2001).
105 The surface sites measurements have high precision and they are mostly located in remote areas
106 with limited spatial coverage. In order to get accurate estimates in inverse modelling, the spatial
107 and temporal characteristics provided by the observed CO₂ measurements are highly important
108 while running the transport model. The densely observed CO₂ observation network is more
109 important in accurately estimating the surface carbon sources and sinks at finer grid scale in
110 atmospheric inversions. The existing observation network is partially compensated by newly
111 available satellite observations and increasingly by aircraft measurements (Niwa et al., 2012).
112 Compared to research aircrafts, passenger aircraft CO₂ measurements can be done at a much
113 lower cost and could cover large areas (Jiang et al., 2014) and those are collected under two
114 projects namely, the Civil Aircraft for the Regular Investigation of the atmosphere Based on
115 an Instrument Container (CARIBIC) and Comprehensive Observation Network for Trace gases
116 by Airliner (CONTRAIL) since 2005 (Machida et al., 2008; Matsueda et al., 2008) which
117 provide a large coverage of in situ CO₂ data ranging over various latitudes, longitudes, and
118 altitudes. According to Niwa et al. (2011) vertical CO₂ profiles measured by aircrafts provide
119 new constraints on surface flux estimation. The Greenhouse Gases Observing Satellite
120 (GOSAT) in January 2009 and the Orbiting Carbon Observatory-2 (OCO-2) satellite in 2014
121 was launched by National Aeronautics and Space Administration (NASA), Atmospheric CO₂
122 observations from space (ACOS) project to capture the CO₂ global distribution at a finer spatial
123 and temporal resolution. The CO₂ measurements collected under various platforms (eg. surface

124 measurements, CONTRAIL and satellites CO₂ measurements) need the help of statistical
125 analysis to accurately estimate the global carbon fluxes in more finer spatial-temporal
126 resolution in inverse modelling. This large amount of atmospheric CO₂ measurements require
127 advanced data assimilation methods to obtain improved estimates at finer scales in inverse
128 modelling (Chatterjee, 2012). In order to address the increasing computational challenges in
129 atmospheric inverse modelling an alternative assimilation techniques for the batch inversions
130 such as Ensemble Kalman Filter (EnKF) (Chatterjee et al., 2012; Feng et al., 2009; Kang et al.,
131 2011; Kim et al., 2014; Miyazaki et al., 2011; Peters et al., 2005, 2007), variational methods
132 (Baker et al., 2006; Basu et al., 2013) and hybrid approaches such as Maximum Likelihood
133 Ensemble Filter (MLEF; Lokupitiya et al., 2008; Zupanski et al., 2007) have been used by the
134 carbon research community to estimate carbon fluxes.

135

136 Although the literature is rich on inverse modelling studies using flask and continuous
137 measurements, only few studies have focused on CO₂ flux estimation using CONTRAIL CO₂
138 measurements with advanced data assimilation methods. Bayesian synthesis inversion has been
139 applied in carbon flux estimation with newly available CONTRAIL CO₂ data in many studies
140 (Jiang et al., 2014; Niwa et al., 2012). Niwa et al. (2012) has performed an inversion study
141 using CONTRAIL measurements in addition to the surface measurement data set
142 (GLOBALEVIEW-CO₂). They have estimated regional monthly surface fluxes using the
143 Bayesian synthesis approach for the period 2006-2008 using the Nonhydrostatic Icosahedral
144 Atmosphere Model-based Transport Model and 64% of error reduction were obtained for
145 tropical Asia regions. Jiang et al. (2014) also used Bayesian synthesis approach with TM5
146 transport model to obtain flux estimates for China using CONTRAIL observations during
147 2002-2008. The results of the study showed that carbon sink in China has increased due to the
148 effect of adding new CONTRAIL CO₂ data and it has decreased the carbon sink in South and
149 Southeast Asia. There are few number of studies used ensemble data assimilation method and
150 obtained satisfactory results (Miyasaki et al., 2011, Zhang et al., 2014) with CONTRAIL CO₂
151 measurements in carbon flux estimation. An inverse modelling system based on CarbonTracker
152 frame work was used by Zhang et al. (2014) to estimate the carbon flux for Asia by introducing
153 CONTRAIL CO₂ measurements and shown that adding CONTRAIL CO₂ can reduce the
154 uncertainty by 11% over the Asian region. Patra et al. (2011) conducted an inversion using
155 CARIBIC data with GLOBALVIEW-CO₂ for year 2008 and simulated CO₂ were evaluated
156 with CONTRAIL CO₂ measurements. In this study, TDI64 time-dependent inverse model and
157 ACTM forward transport simulations were used for the flux estimation. During 2008, it was
158 identified that the net CO₂ uptake of 0.37 ± 0.20 Pg C yr⁻¹ by the South Asian region. Miyazaki
159 et al. (2011) has developed an advanced 4-D data assimilation system based on (Ensemble
160 Kalman Filter) EnKF with a 3 day assimilation window to estimate surface CO₂ fluxes at model
161 grid point using three types of atmospheric measurements such as GOSAT, CONTRAIL and
162 ground surface. According to the results of this study, a large flux error reductions in the
163 continental areas of the northern extra tropics were occurred due to surface network data and
164 GOSAT contributed to a large error reduction over North and South America, South Africa,
165 and Temperate and Boreal Asia. And the large error reduction over Europe and Tropical and
166 Temperate Asia were due to CONTRAIL data.

167

168 As described above, only a handful of studies have been done in the past on global scale CO₂
169 fluxes. In the current study, we estimate the global scale carbon fluxes for years 2009-2011 by
170 using an ensemble-based data assimilation system known as MLEF (Lokupitiya et al., 2008;
171 Zupanski, 2005; Zupanski et al., 2007). The method have been tested for existing flask and in-
172 situ CO₂ observations using a pseudodata experiment by Lokupitiya et al. (2008). MLEF is an
173 ensemble based data assimilation method based on maximum likelihood and Ensemble data

174 assimilation and it has the capability of handling large observational vectors. Not like in
175 variational data assimilation method (Baker et al., 2006, Chevallier et al., 2005) it can be used
176 with non-linear observation operators and no need to calculate model adjoints (i.e. calculation
177 of backward-in-time transport). Fixed-lag Kalman smoother introduced by Bruhwiler et al.
178 (2005), steps through the observations sequentially, avoids the difficulties of using large
179 observation vectors in batch mode method. But pre-calculation of observation operators is
180 much expensive when assimilating hourly large observation vectors (Lokupitiya et al., 2008).
181 The optimal solution obtained using other ensemble data assimilation methods is a minimum
182 variance solution but MLEF gives an optimal solution based on maximum likelihood solution.
183 Since, MLEF algorithm is based on maximum likelihood estimation the additional calculation
184 required for the iterative minimization can be negligible, compared to the cost of ensemble
185 forecast and Hessian preconditioning calculations (Zupanski, 2005). This property provides a
186 grate advantage for data assimilation problems with large observation vectors like CONTRAIL
187 CO₂ data. Serial processing of observations is not used in covariance localization under MLEF
188 method. Like other ensemble data assimilation methods, MLEF uses ensembles in calculating
189 error covariance matrix and these ensembles efficiently calculate Hessian preconditioning and
190 the gradient of the cost function. Multiple process capability of parallel computing is used in
191 order to optimize the MLEF performance in realistic applications and this significantly reduced
192 the computational cost (Zupanski, 2005). When comparing with computational cost, both
193 variational and ensemble methods are similar. But the great advantage of the ensemble method
194 is that it is more efficient in parallel computing environment (Lokupitiya et al., 2008). This
195 study is the first time, the MLEF algorithm is used in the inverse modelling approach with
196 CONTRAIL CO₂ measurements.

197

198 In this study, MLEF algorithm was developed to assimilate CONTRAIL measurements. We
199 have previously tested this assimilation system in a pseudodata experiment by considering the
200 in-situ CO₂ measurement network and CONTRAIL observations (Perera et al., 2017). We
201 obtained satisfactory results for the densely observed regions such as North America, Europe
202 and Asia. This paper presents the first application of the MLEF method to recover fluxes by
203 using the actual CO₂ measurements from flasks, continuous sites and CONTRAIL. The
204 optimized CO₂ fluxes by assimilating the actual flask, continuous and CONTRAIL CO₂
205 measurements were obtained for the years from 2009 to 2011. We compared our results with
206 those of CarbonTracker (Peters et al., 2005, 2007, CT2017 release at
207 <https://www.esrl.noaa.gov/gmd/ccgg/carbontracker/CT2017/>).

208

209 The paper is organized as follows. Method is described in Section 2. MLEF data assimilation
210 method and observation vector used for the data assimilation are discussed here. In section 3,
211 we present and compare our results with pervious findings. Finally, section 4 provides the
212 concluding remarks and future directions.

213

214 **2 Materials and Methods**

215 **2.1 MLEF**

216

217 The MLEF has been developed by combining ideas from variational methods, iterated Kalman
218 filters, and the ensemble transform Kalman filter (Lokupitiya et al., 2008; Zupanski, 2005).
219 Unlike other ensemble-based methods, the MLEF incorporates iterative minimization of a non-
220 linear cost function with advanced Hessian preconditioning, which makes it more robust for
221 non-linear processes. The method is based on maximum likelihood (rather than minimum

222 variance) estimation and thus the optimal solution is given by the mode (rather than the mean)
 223 of the posterior distribution. Hence the MLEF can produce robust estimates even when the flux
 224 distribution deviates from the Gaussian assumption, as shown in Zupanski et al. (2007).

225

226 **2.2 Atmospheric Transport Model**

227

228 Inverse modeling for carbon fluxes requires a transport model to simulate 3-D CO₂
 229 concentrations, from which we sample the CO₂ at the locations (i.e. for a specific latitude,
 230 longitude and elevation) and times of the observations. This serves as the observation operator
 231 in the data assimilation scheme. The observation operator performs the necessary interpolations
 232 and transformations from the state variable to the observation space.

233

234 In this study, we used the Parameterized Chemistry Transport Model (PCTM) (Kawa et al.,
 235 2004) driven by weather data from the MERRA2 meteorological fields based on the Goddard
 236 Earth Observation System Model, version 2, by the NASA Global Modeling and Assimilation
 237 Office (GAMO). The PCTM model has been used in CO₂ assimilation studies as an observation
 238 operator by Lokupitiya et al. (2008) and Zupanski (2005) and showed reasonable results with
 239 continuous and flask CO₂ measurements. Perera et al. (2017) compared the model results with
 240 CONTRAIL measurements in addition to the existing flask and continuous measurements and
 241 showed similar results for the carbon flux estimation in densely observed areas.

242

243 All the data collections from MERRA2 are provided on the same horizontal grid which has
 244 576 points in the longitudinal direction and 361 points in the latitudinal direction,
 245 corresponding to a resolution of 0.625°×0.5°. In MERRA2 the variables are provided on
 246 vertical grid with 72 model layers or the 73 edges, in the altitude range of 0-50 km. The weather
 247 data files (three-hourly time-averaged files) contain averages over time intervals centered and
 248 time stamped at 01:30 GMT, 04:30 GMT, and 07:30 GMT (Bosilovich et al., 2016).

249

250 In this study, the PCTM was run at 2.5° longitude by 2.0° latitude horizontal resolution with
 251 25 vertical levels, in the altitude range of 0-22 km. The model integration time step was chosen
 252 as 15 minutes. The resolution of the wind and diagonals, which are derived from MERRA2
 253 weather product, have been regridded to coarser 2.5°×2.0° resolution.

254

255 **2.3 Data Assimilation scheme**

256 **2.3.1 Mathematical formulation of the carbon flux**

257 We estimated multiplicative biases in photosynthesis, respiration, and air-sea gas exchange
 258 using our data assimilation system. Variations of the surface flux of CO₂ can be mathematically
 259 represented across each of our assimilation windows as follows:

$$\begin{aligned}
 F(x, y, t) = & [1 + \beta_{RESP}(x, y)]RESP(x, y, t) - [1 + \beta_{GPP}(x, y)]GPP(x, y, t) \\
 & + [1 + \beta_{Ocean}(x, y)]Ocean(x, y, t) + FF(x, y, t),
 \end{aligned}
 \tag{1}$$

260

261

262 where, F - carbon flux, $RESP$ is the ecosystem respiration, GPP is the gross primary
 263 productivity, $Ocean$ represents air-sea gas exchange of CO₂, and FF represents emissions due
 264 to fossil fuel combustion; x and y denote the spatial coordinates and t represents the time. The
 265 β 's represent multiplicative biases of the grid-scale component fluxes which are assumed to
 266 persist for longer periods of time than the fluxes themselves (Lokupitiya et al., 2008; Schuh et
 267 al., 2010; Zupanski et al., 2007). Equation (1) represents the optimization for a given data

268 assimilation cycle. Here we do not include the time (t) variable for β 's because they are
269 assumed to be constant within the data assimilation cycle. Hourly land fluxes ($RESP$ and GPP)
270 are derived at each grid cell from the Simple Biosphere-version 3 (SiB3) model (Baker et al.,
271 2003). Ocean fluxes are from Takahashi et al. (2002) and fossil fuel (FF) emissions from
272 Brenkert (1998). Mean annual FF emissions of 1998 were linearly scaled for the years 2009,
273 2010 and 2011 to produce the FF maps. We did not include biomass burning in our priors;
274 hence the impact from biomass burning is embedded in the other flux estimates. Biases are
275 solved for at a coarser 2.5° longitude by 2° latitude spatial resolution, whereas fluxes and
276 transport are gridded at 2.5° longitude by 2° latitude spatial resolution. At the coastlines, grid
277 boxes are assigned to either land or ocean based on the percentage of coverage. The coarser
278 grid for biases is chosen to reduce the number of unknowns in the problem.

279
280 Here we solve for monthly variations of biases in GPP , $RESP$, and $Ocean$ fluxes (β_{GPP} , β_{RESP} ,
281 β_{Ocean}) and for the purpose of this paper, we assume that $\beta_{FF} = 0$. Trial values for the different
282 ensemble runs at every model grid cell in each of these three flux components are selected from
283 a distribution to construct a global map of the β 's for each ensemble member. These maps of
284 β 's are then multiplied by the flux computed from the forward model at each model time step
285 that the transport operator (PCTM) is applied and then sampled to yield an ensemble of CO_2
286 mixing ratio time series at each observation station associated with each candidate map. An
287 eight-week time series of hourly observations is thereby constructed for each ensemble
288 member, after which time optimal values of the biases are estimated for each grid cell by
289 comparison to the real observations.

290
291 Simulated variations of $GPP(x,y,t)$ and $RESP(x,y,t)$ due to diurnal, synoptic, and seasonal
292 variations are explicitly represented using mechanistic models, and spatially resolved
293 multiplicative biases are separately estimated for each component flux. Sub-daily variations in
294 the simulated component fluxes $RESP$ and GPP are primarily controlled by the weather
295 (especially changes in radiation due to clouds and the diurnal cycle of solar forcing), whereas
296 seasonal changes are derived from phenological calculations parameterized from satellite
297 imagery. Fine scale spatial variations are driven by changes in vegetation cover, soil texture,
298 and soil moisture. A persistent bias in photosynthesis might result (for example) from
299 underestimation of available nitrogen, forest management, or agricultural land-use, whereas a
300 persistent bias in respiration might result from overestimation of soil carbon or coarse woody
301 debris. In any case, it is reasonable to assume that the biases β_{RESP} and β_{GPP} vary more slowly
302 than the fluxes themselves.

303 304 **2.3.2 Data assimilation window**

305
306 Size of the data assimilation window represents how far back in time we expect to be able to
307 locate a given flux signal from available measurements (CT2017 release at
308 <https://www.esrl.noaa.gov/gmd/ccgg/carbontracker/CT2017/>). In this study, an 8-week data
309 assimilation window is used for the estimation of the β 's, and each 8-week window overlaps
310 the previous window by 4 weeks.

311 312 313 **2.3.3 Initial guess of the biases and propagation of the error covariance matrix**

314
315 The data assimilation process has been started from the unbiased case (i.e. $\beta_s = \mathbf{0}$). Prior
316 uncertainty for land components ($GPP/RESP$) and ocean are prescribed as 20% and 10%,
317 respectively, at the first data assimilation cycle at the starting time. Here, these are applied

318 separately to the gross fluxes, not for the net difference (i.e. $GPP - RESP$) between them.
 319 Large prior uncertainties may allow more freedom for the biases to move. The use of such
 320 priors needs dense observation network in order to find an optimal solution. Smaller prior
 321 uncertainties may lead biases to get stuck in a wrong solution. The choice of prior uncertainties
 322 is arbitrary. Ocean biases are allowed very minor changes. Therefore the results can be well
 323 interpreted only for well-observed land regions and cannot make quantitative flux estimates for
 324 other land regions or the oceans.

325
 326 In MLEF, for each subsequent cycle, prior and the covariance of the biases have to be defined.
 327 That is, we define the center value for the estimate and its variability by an analysis covariance
 328 matrix from the previous cycle to condition the distribution from which candidate β s are
 329 selected at each grid cell for each ensemble member of the next cycle. In MLEF, the average
 330 of posterior from previous cycle and prescribed values from the initial cycle is considered as
 331 the prior. Hence, according to our assumption, the average of the previous analysis state and
 332 the forecast state in the initial cycle becomes the prior state for the next cycle. Similarly, the
 333 uncertainty of the biases, which is the covariance matrix of the biases also needed to be defined.
 334 In the case of unreasonably smaller values of the error covariance, the perturbations used to
 335 generate each ensemble member would become very small and the β s could converge to
 336 incorrect values. To avoid this problem, the covariance matrix is “inflated” in each new cycle.
 337 In MLEF, covariance inflation was done by applying a higher weight (= 0.9) for the initial
 338 covariance as given in Equation (2).
 339

$$340 \text{ Prior covariance for the current cycle} = (0.1 \times \text{analyzed covariance from previous cycle}) + \\
 341 \qquad \qquad \qquad (0.9 \times \text{initial covariance}) \qquad \qquad \qquad (2)$$

342
 343 In the case of an under-determined problem, an optimal solution can only be reached when the
 344 ensemble size is very large. However, larger ensemble sizes involve high computational cost.
 345 Hence smoothing and localization schemes have been applied to alleviate the problems of
 346 sparse sampling. Covariance smoothing is introduced only in the first data assimilation cycle
 347 according to an exponential decay function (Lokupitiya et al., 2008; Michalak et al, 2004;
 348 Peters et al., 2005; Rödenbeck et al., 2003). In this study, we chose to smooth the prescribed
 349 covariance in the initial assimilation cycle with an e-folding length of 800 km over the land
 350 points and 1600 km over the ocean points.

351
 352 Subsequently, we introduced a localization scheme, which is sensitive to dynamical changes
 353 in the posterior (analysis) and prior (forecast) uncertainties (Lokupitiya et al., 2008; Zupanski
 354 et al., 2007). To define the “distance” for covariance localization, we employed the ratio r
 355 between the prior (σ_{Prior}) and the posterior ($\sigma_{Posterior}$) uncertainty of the current cycle defined as
 356 $r = \sigma_{Prior} / \sigma_{Posterior}$. The greater values of the ratio represent the areas with the greater influence
 357 from the observations. We set the influence regions based on the distribution of the ratio r . We
 358 restricted adjustments to model biases to the 40% of land points and 10% of ocean points best
 359 constrained by the observations, based on the upper tail values of the ratio probability
 360 distribution. This choice selects the densely observed regions. Only these selected regions are
 361 allowed to change from the prior mean. The forward model is run with the revised biases to
 362 produce the 3-D CO_2 fields for the next assimilation cycle. CarbonTracker uses a localization
 363 scheme based on the correlation coefficient between the parameter deviations and the
 364 observation deviations. Cut-off values are selected according to the two-tailed student’s T -test,
 365 at 95% significance level (Peters et al., 2007).
 366
 367
 368

369 **2.3.4 Ensemble size**

370

371 In order to determine the adequate ensemble size, Lokupitiya et al. (2008) and Zupanski et al.
 372 (2007) used an information measure referred to as Degrees of Freedom for Signal (DFS).
 373 Given the number of observations and the ensemble size, DFS being a positive integer indicates
 374 whether the selected ensemble size was appropriate (Lokupitiya et al., 2008). In this study, we
 375 used 90 ensemble members for the data assimilation.

376

377 **2.4 CO₂ observation network used for data assimilation**

378

379 We assimilated flask and continuous observations obtained from the existing observation
 380 networks (see Figure 1 and Table 1) and CONTRIAL CO₂ measurements (see Figure 9) for the
 381 years from 2009 to 2011. Flask and continuous observations are collected near the surface. The
 382 temporal variation in the vertical structure is still relatively limited through these observations.
 383 This may result an incomplete view of the three-dimensional temporal variation of atmospheric
 384 CO₂. However, research aircraft measurements can provide vertical and horizontal
 385 distributions of CO₂ with sufficient precision to validate transport models, as well as being
 386 useful in providing an increased level of constraint in carbon flux estimates by inverse
 387 modelling (Sawa et al., 2012).

388

389 **Table 1.** Continuous and Flask CO₂ measurement sites used in this study

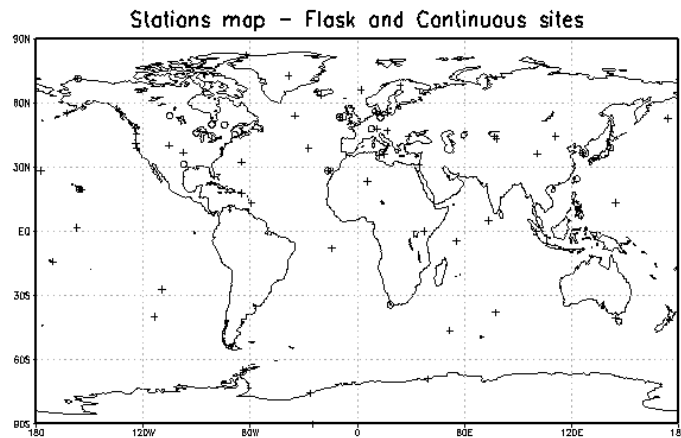
390

Site Name	Latitude	Longitude	Elevation	Observation error		
				2009	2010	2011
Air samples collected in glass flasks						
Alert, Nunavut, Canada (ALT)	82.45	-62.51	0	3.39	3.18	5.16
Amsterdam Island, France (AMS)	-37.95	77.53	0	2.00	2.00	2.00
Ascension Island, United Kingdom (ASC)	-7.97	-14.40	0	2.89	2.35	2.25
Assekrem, Algeria (ASK)	23.26	5.63	2710	2.24	2.55	2.87
St. Croix, Virgin Islands, United States (AVI)	17.75	-64.75	0	2.00	2.00	2.00
Terceira Island, Azores, Portugal (AZR)	38.77	-27.38	0	1.85	1.49	3.87
Baltic Sea, Poland (BAL)	55.35	17.22	0	9.64	9.85	6.66
Baring Head Station, New Zealand (BHD)	-41.41	174.87	0	2.57	2.54	2.51
Bukit Kototabang, Indonesia (BKT)	-0.20	100.32	0	6.28	6.27	4.36
St. Davids Head, Bermuda, United Kingdom (BME)	32.37	-64.65	0	4.51	2.28	2.00
Tudor Hill, Bermuda, United Kingdom (BMW)	32.26	-64.88	0	3.42	3.63	3.99
Barrow Atmospheric Baseline Observatory, United States (BRW)	71.32	-156.61	0	4.51	4.43	5.88
Black Sea, Constanta, Romania (BSC)	44.18	28.66	0	15.87	15.39	15.85
Cold Bay, Alaska, United States (CBA)	55.21	-162.72	0	3.39	3.73	5.28
Cape Grim, Tasmania, Australia (CGO)	-40.68	144.69	0	2.86	2.83	2.66
Christmas Island, Republic of Kiribati (CHR)	1.70	-157.15	0	1.57	1.52	1.72
Cape Meares, Oregon, United States (CMO)	45.48	-123.97	0	2.00	2.00	2.00
Crozet Island, France (CRZ)	-46.43	51.85	0	2.94	2.83	3.34
Easter Island, Chile (EIC)	-27.15	-109.45	0	2.79	2.78	2.69
Mariana Islands,Guam (GMI)	13.39	144.66	0	1.72	2.11	2.22
Dwejra Point, Gozo, Malta (GOZ)	36.05	14.89	0	2.00	2.00	2.00
Halley Station, Antarctica, United Kingdom (HBA)	-75.61	-26.21	0	8.83	8.61	9.30
Hohenpeissenberg, Germany (HPB)	47.80	11.02	0	9.47	10.00	10.06
Hegyhatsal, Hungary (HUN)	46.95	16.65	0	11.31	10.12	13.30
Storhofdi, Vestmannaeyjar, Iceland (ICE)	63.40	-20.29	0	3.04	2.00	2.00
Izana, Tenerife, Canary Islands, Spain (IZO)	28.30	-16.48	2373	2.20	2.38	3.03
Kaashidhoo, Republic of Maldives (KCO)	4.97	73.47	0	2.00	2.00	2.00
Key Biscayne, Florida, United States (KEY)	25.67	-80.20	0	2.95	3.13	3.22
Cape Kumukahi, Hawaii, United States (KUM)	19.52	-154.82	0	2.16	2.65	3.39
Sary Taukum, Kazakhstan (KZD)	44.08	76.87	0	7.80	2.00	2.00
Plateau Assy, Kazakhstan (KZM)	43.25	77.88	2519	5.36	2.00	2.00
Lampedusa, Italy (LMP)	35.52	12.62	0	3.66	3.54	4.46
Mace Head, County Galway, Ireland (MHD)	53.33	-9.90	0	3.74	3.91	4.63
Sand Island, Midway, United States (MID)	28.21	-177.38	0	2.57	3.02	4.12
Mt. Kenya, Kenya (MKN)	-0.06	37.30	3644	3.12	3.63	2.28

Table 1. (Continued)						
Mauna Loa, Hawaii, United States (MLO)	19.54	-155.58	3397	1.91	2.37	2.26
Niwot Ridge, Colorado, United States (NWR)	40.05	-105.58	3523	3.40	3.73	4.51
Olympic Peninsula, Washington, United States (OPW)	48.30	-124.63	0	2.00	2.00	2.00
Pallas-Sammaltunturi, GAW Station, Finland (PAL)	67.97	24.12	0	8.04	6.46	6.94
Palmer Station, Antarctica, United States (PSA)	-64.92	-64.00	0	7.35	7.61	7.69
Point Arena, California, United States (PTA)	38.95	-123.73	0	5.91	6.37	7.75
Ragged Point, Barbados (RPB)	13.17	-59.43	0	2.20	2.49	2.97
Mahe Island, Seychelles (SEY)	-4.68	55.53	0	1.68	1.31	1.74
Southern Great Plains, Oklahoma, United States (SGP)	36.80	-97.50	0	13.82	10.24	8.68
Shemya Island, Alaska, United States (SHM)	52.72	174.10	0	3.53	3.73	6.07
Tutuila, American Samoa (SMO)	-14.25	-170.56	0	1.31	0.88	1.10
South Pole, Antarctica, United States (SPO)	-89.98	-24.80	0	10.96	12.23	12.31
Ocean Station Charlie, United States (STC)	54.00	-35.00	0	2.00	2.00	2.00
Ocean Station M, Norway (STM)	66.00	2.00	0	4.63	2.00	2.00
Summit, Greenland (SUM)	72.60	-38.42	3209	2.93	2.79	5.01
Syowa Station, Antarctica, Japan (SYO)	-69.00	39.58	0	4.04	3.87	3.91
Tae-ahn Peninsula, Republic of Korea (TAP)	36.73	126.13	0	5.82	5.94	6.69
Trinidad Head, California, United States (THD)	41.05	-124.15	0	4.68	5.12	6.67
Wendover, Utah, United States (UTA)	39.90	-113.72	0	4.44	4.49	3.70
Ulaan Uul, Mongolia (UUM)	44.45	111.10	0	3.61	3.54	5.48
Weizmann Institute of Science at the Arava Institute, Ketura, Israel (WIS)	30.86	34.78	0	3.60	3.41	5.26
Mt. Waliguan, Peoples Republic of China (WLG)	36.29	100.90	0	3.31	3.28	3.87
Ny-Alesund, Svalbard, Norway and Sweden (ZEP)	78.90	11.89	0	3.68	3.43	5.44
Continuous In-situ CO₂ analyzer from Towers.						
Argyle, Maine, United States (AMT)	45.03	-68.68	107	10.48	9.59	9.25
lef011 - Park Falls, Wisconsin, United States (LEF)	45.94	-90.27	11	9.36	2.00	2.00
lef030	45.94	-90.27	30	11.10	8.08	10.30
lef076	45.94	-90.27	76	7.59	2.00	2.00
lef122	45.94	-90.27	122	8.17	6.89	9.43
lef244	45.94	-90.27	244	4.90	2.00	2.00
lef396	45.94	-90.27	396	6.93	6.45	8.89
wkt009 - Moody, Texas, United States (WKT)	31.32	-97.33	9	2.00	2.00	2.00
wkt030	31.32	-97.33	30	8.15	7.90	6.77
wkt061	31.32	-97.33	61	2.00	2.00	2.00
wkt122	31.32	-97.33	122	6.77	6.90	6.35
wkt244	31.32	-97.33	244	2.00	2.00	2.00
wkt457	31.32	-97.33	457	4.96	5.56	5.39
In-situ co2 hourly averages						
Mauna Loa, Hawaii, United States (MLO)	19.54	-155.58	3397	1.97	2.37	2.23
Barrow Atmospheric Baseline Observatory, United States (BRW)	71.32	-156.61	11	4.49	4.17	5.95
Anmyeon-do, Republic of Korea (AMY)	36.54	126.33	46	8.50	8.19	8.01
Candle Lake, Canada (CDL)	53.99	-105.12	600	5.34	5.55	2.00
Chibougamau, Canada (CHM)	49.69	-74.34	393	4.75	4.78	6.37
Cape Point, South Africa (CPT)	-34.35	18.49	230	2.96	2.72	2.86
Fraserdale, Canada (FSD)	49.86	-81.57	210	5.96	6.00	7.19
Izaña (Tenerife), Spain (IZO)	28.31	-16.50	2373	2.18	2.36	3.13
Mace Head, Ireland (MHD)	53.33	-9.90	5	5.43	5.43	6.48
Neuglobsow, Germany (NGL)	53.14	13.03	62	14.46	15.73	16.62
Ryori, Japan (RYO)	39.03	141.82	260	7.82	8.92	7.09
Schauinsland, Germany (SSL)	47.90	7.92	1205	6.94	7.79	6.74
Yonagunijima, Japan (YON)	24.47	123.01	30	4.73	5.33	5.46
Zeppelin Mountain (Ny Ålesund), Norway (ZEP)	78.91	11.89	475	3.92	3.49	5.20

391

392



405
 406 **Figure 1.** A map of the continuous and flask stations used in this study except CONTRAIL.
 407 Open circles depict continuous measurement sites (see Table 1). Crosses identify flask-
 408 sampling locations that are part of the NOAA-ESRL network (GLOBALVIEW-CO₂).
 409

410
 411

412 **2.4.1 In-situ CO₂ measurements**

413

414 Flask and in-situ CO₂ observations used in this study were taken mainly from two observation
 415 networks, GLOBALVIEW-CO₂ and WDCGG (World Data Centre for Greenhouse Gases).
 416 GLOBALVIEW-CO₂ is a product of the Corporate Atmospheric Data Integration Project
 417 coordinated and maintained by NOAA ESRL (National Oceanic and Atmospheric
 418 Administration, Earth System Research Laboratory). NOAA provides high-quality CO₂
 419 measurements collected from multiple institutions (<https://www.esrl.noaa.gov/>). WDCGG is a
 420 World Data Centre (WDC) operated by the Japan Meteorological Agency (JMA) under the
 421 Global Atmosphere Watch (GAW) programme of the World Meteorological Organization
 422 (WMO). It collects, archives and distributes data provided by contributors on greenhouse gases
 423 such as CO₂, CH₄, CFC, N₂O and related gases such as CO in the atmosphere and elsewhere
 424 (<https://gaw.kishou.go.jp/>). In this study, the observation vector consists of 58 surface flask
 425 observations sites collected on weekly basis and 27 continuous sites that are measuring in-situ
 426 at different vertical levels on the hourly basis in addition to the CONTRAIL data.

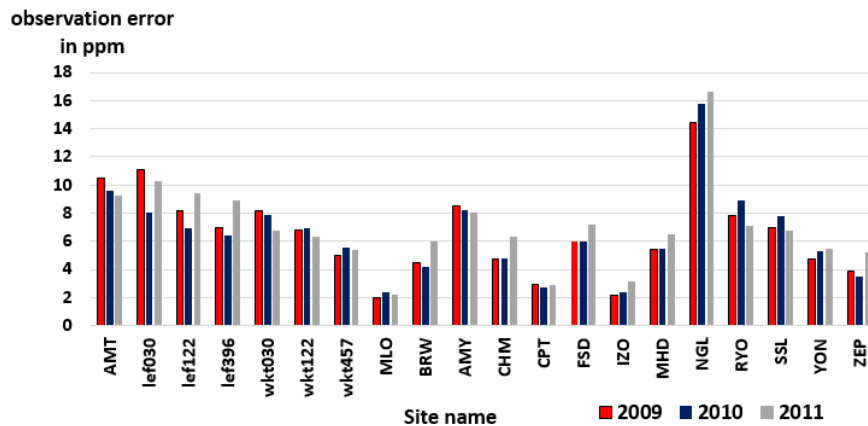
427

428 In this study, the diurnal cycle at continuous sites were filtered according to the local
 429 meteorology. Low-elevation sites (LEF, WKT, MHD) were used during mid-day only (11 to
 430 16 hours local time) because well-developed boundary-layer mixing is better simulated in the
 431 transport model than stable nocturnal conditions or morning and evening transitions.
 432 Mountaintop sites (MLO, IZO and SSL) were used at night (0-4 hours local time), because
 433 subsiding mid-tropospheric air at night better represents model conditions than upslope
 434 conditions during the day. Impact from each observation site varies according to how well
 435 transport model captures the observations at the site. These differences in the transport
 436 represent the diagonal elements of the observation error covariance matrix.

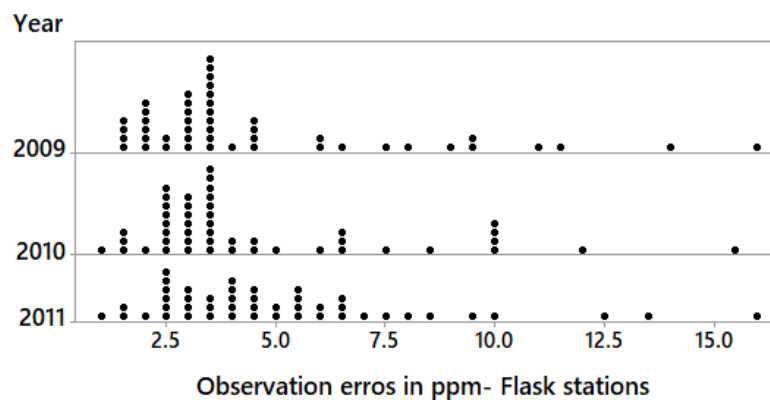
437

438 We computed average model-data mismatch error at each site as the observation error, by
 439 running transport model (PCTM) separately for the years 2009-2011 (Table 1). Observation
 440 errors at the multi-level observation stations such as LEF and WKT vary according to the height
 441 of the measurement levels. When compared with other continuous sites, station NGL shows
 442 the highest observation error for each year (Figure 2). Errors at the flask stations vary between

443 the minimum and the maximum values of 1.31 ppm - 15.87 ppm, 0.88 ppm – 15.39 ppm and
 444 1.1 ppm – 15.85 ppm for the years 2009, 2010, and 2011, respectively (Figure 3).
 445



458
 459 **Figure 2.** Variation of the observation errors for Continuous stations for the years 2009-2011.
 460

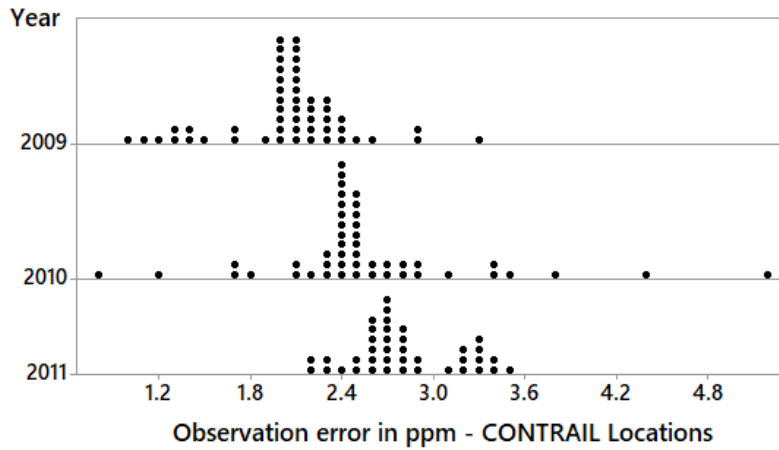


461
 462
 463
 464
 465
 466
 467
 468
 469
 470
 471
 472 **Figure 3.** Variation of the observation errors for Flask stations for the years 2009-2011.
 473

474
 475 **2.4.2 CONTRAIL CO₂ measurements**

476
 477 In order to achieve a better global view of the three-dimensional variations in CO₂
 478 measurements, CONTRAIL measurements were also used in this study. Five “JAL” air planes
 479 on regular commercial service measure CO₂ continuously during each flight. In addition to the
 480 vertical profiles of CO₂ during ascent and descent, horizontal measurements are obtained along
 481 the flight path. The aircraft measurements cover a substantial geographical region, with a wide
 482 longitudinal coverage (0°E–115°W) in mid-latitudes to high latitudes in Northern Hemisphere.
 483 The CONTRAIL observation extends in the north-south direction, along the various JAL
 484 flights between Japan, Australia and Southeast Asia. This observation provides regional
 485 vertical/upper atmospheric CO₂ data over extensive areas in the Eurasian continent, Tropical
 486 region and the Southern Hemisphere where the number of surface stations are limited
 487 (<http://www.cger.nies.go.jp/contrail/index.html> access: 01 August 2019). The flights cover the
 488 area 30S- 50N and 60-160E (Figure 9). Model data mismatch errors for CONTRAIL locations
 489 are shown in Figure 4.
 490

491
 492
 493



507 **Figure 4.** Variation of the observation errors for CONTRAIL locations for the years 2009-
 508 2011.

509
 510

511 **2.5 Model comparison with Carbon Tracker**

512

513 We compared our results with CarbonTracker (CT2017), another ensemble-based data
 514 assimilation system (Peters et al., 2005, 2007, CT2017 release at
 515 <https://www.esrl.noaa.gov/gmd/ccgg/carbontracker/CT2017/>), which has been developed
 516 based on the fixed-lag Kalman smoother (Bruhwiler et al., 2005) and ensemble square root
 517 filter (Whitaker & Hamill, 2002). CT2017 uses multiple in-situ observation networks and prior
 518 models to optimize weekly fluxes over 126 land “ecoregions” and 30 ocean regions (Peters et
 519 al., 2007; https://www.esrl.noaa.gov/gmd/ccgg/carbontracker/CT2017_doc.php, last acces:16
 520 August 2019). CT2017 uses TM5 transport model which connects the surface fluxes to
 521 atmospheric CO₂ mole fractions. The model uses measurements of air samples collected at 254
 522 sites around the world by 55 laboratories and assimilates hourly average CO₂ concentrations.
 523 CT2017 uses two biosphere models, which provide first-guess terrestrial fluxes. CASA
 524 (Carnegie-Ames Stanford Approach) calculates global carbon fluxes using input from weather
 525 models to drive biophysical processes, and satellite observed Normalized Difference
 526 Vegetation Index (NDVI) to track plant phenology. Global Fire Emissions Database Version
 527 4.1 (GFEDv4) is used as one of the fire modules to estimate biomass burning, and
 528 climatological estimates of CO₂ partial pressure in surface waters (pCO₂) from Takahashi et
 529 al. (2002) is used as the first-guess of air-sea flux. In CT2017, observed-minus-forecasted mole
 530 fraction that exceeds 3 times the prescribed model-data mismatch has been considered as an
 531 indicator that the modeling framework fails. The scaling factors λ are estimated independently
 532 for each week and optimization region using a moving overlapping assimilation window.
 533 CarbonTracker solves for fluxes by considering multiplicative scaling factors (biases) in NEE
 534 and air-sea gas exchange. CarbonTracker uses 150 ensemble members in their flux estimation.

535

536 **3 Results and Discussion**

537 This section is organized as three parts: performance of the transport model in simulating the
 538 CO₂ concentrations, characteristics of the optimized CO₂ fluxes (biosphere and ocean) using
 539 MLEF for the years 2009-2011 and comparison of the MLEF results with other studies mainly
 540 over the North America, Europe, Asia and Australia.

541

542 **3.1 Evaluation of the transport model simulation**

543

544 We checked the performance of PCTM model by comparing model simulated CO₂ with the
 545 observed CO₂ at observation network used in this study which consists of flask, continuous and
 546 CONTRAIL measurements. After a three-year spin-up from years 2006-2008, CO₂ at
 547 observation stations were sampled for years 2009-2011. For the comparison with actual CO₂
 548 measurements, a global constant off-set values have been added at each observation station.
 549 Figure 5 shows a comparison between PCTM simulated CO₂ and the actual CO₂ measurements
 550 at the continuous sites AMT, BRW and FSD for the years from 2009 to 2011.
 551

552

553

554

555

556

557

558

559

560

561

562

563

564

565

566

567

568

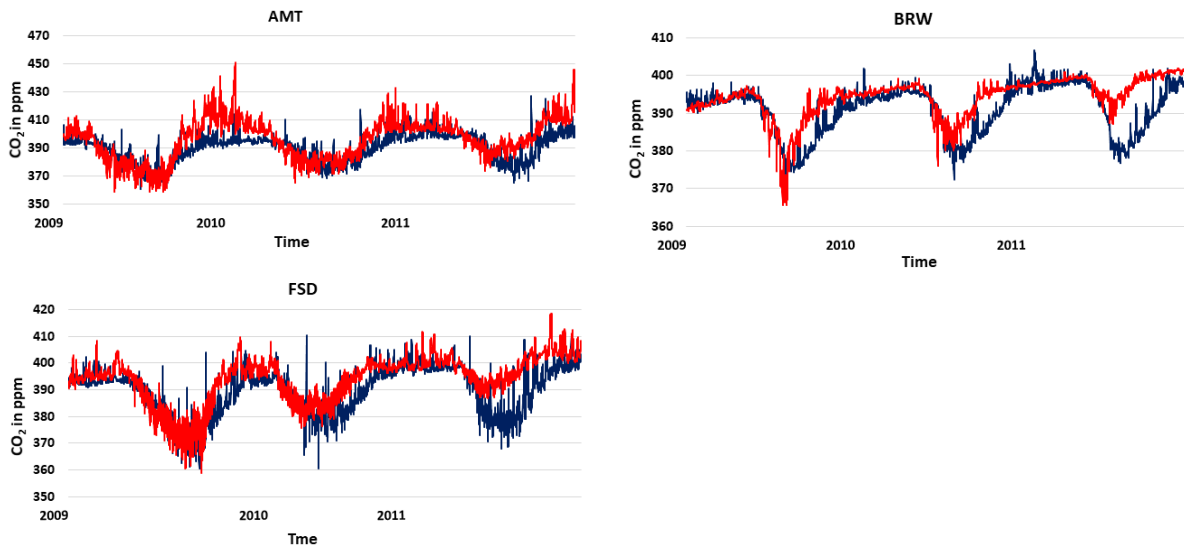
569

570

571

572

573



569 **Figure 5.** Observed hourly CO₂ concentrations (in blue) and simulated CO₂ (in red) from
 570 PCTM for years from 2009 – 2011 at stations FSD (Fraserdale, Canada), AMT
 571 (Argyle, Maine, United States) and BRW (Barrow Atmospheric Baseline
 572 Observatory, United States).
 573

574 Observation error for each observation site is calculated by averaging the difference between
 575 observed values (actual CO₂) and the PCTM simulated CO₂ values throughout the year.
 576 Observation errors for the flask and continuous sites for the years 2009-2011 are given in Table
 577 1. Figures 2 and 3 summarize the variation of the observation errors (actual – simulated) from
 578 2009-2011 for each continuous site and flask station. According to the above results, site
 579 “NGL” in Germany shows the highest observation error in each year. When compared with all
 580 other sites, “MLO”, “CPT”, “IZO” and “ZEP” show relatively low observation errors. For the
 581 flask stations, observation errors vary from 0.88 ppm to 16.0 ppm. Variation of the observation
 582 errors for the CONTRAIL locations are shown in Figure 4. Observation errors of CONTRAIL
 583 locations show considerably small values than flask and continuous stations. The average and
 584 uncertainty of the observation errors are 2.04 ± 0.43 ppm, 2.56 ± 0.71 ppm and 2.81 ± 0.36
 585 ppm for the years 2009, 2010, and 2011, respectively. According to above results, simulated
 586 CO₂ using PCTM shows good agreement with the flask and continuous measurements as well
 587 as the CONTRAIL measurements.
 588
 589
 590
 591

592 **3.2 Forward model comparisons**

593

594 We used forward model comparisons to test the quality of the data assimilation. Figure 6 shows
 595 observed daily mean CO₂ concentrations along with the daily mean recovered and prior CO₂
 596 concentrations obtained from optimized (posterior) fluxes and prior fluxes at North American
 597 stations (Argyle, Maine, United States (AMT), Barrow Atmospheric Baseline Observatory,
 598 United States (BRW), Chibougamau, Canada (CHM)) and several stations in Asian region
 599 (Ryori, Japan (RYO), Anmyeon-do, Republic of Korea (AMY) and Yonagunijima, Japan
 600 (YON)) for the years 2009 to 2011.

601

602

603

604

605

606

607

608

609

610

611

612

613

614

615

616

617

618

619

620

621

622

623

624

625

626

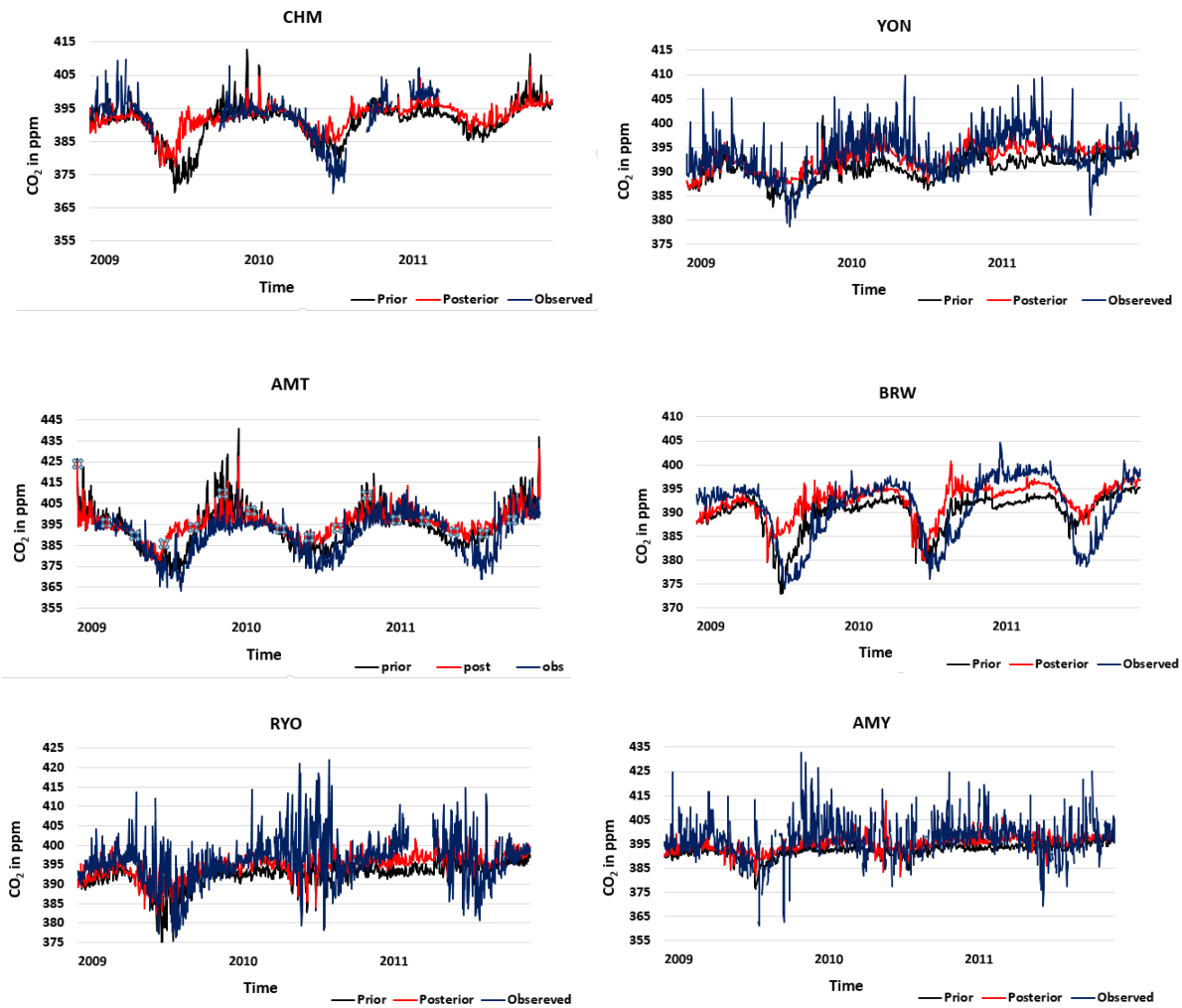
627

628

629

630

631



632

633

634

635

636

637

638

639

640

Figure 6. Daily time series plots of CO₂ concentrations from posterior fluxes (in red) and prior fluxes (in black) compared to observations (in blue) for years 2009 – 2011 at Yonagunijima, Japan (YON), Ryori, Japan (RYO), Anmyeon-do, Republic of Korea (AMY), Argyle, Maine, United States (AMT), Chibougamau, Canada (CHM) and Anmyeon-do, Republic of Korea (AMY)

641 **Table 2.** Root Mean Square Error (RMSE) with respect to the prior and the posterior at
 642 continuous sites for 2009 to 2011 Units: parts per million by volume (ppmv)
 643

Station	Latitude (deg)	Longitude (deg)	Elevation (m)	2009			2010			2011		
				RMSE Prior	RMSE Posterior	Difference	RMSE Prior	RMSE Posterior	Difference	RMSE Prior	RMSE Posterior	Difference
AMT	45.03	-68.68	107	9.18	9.82	-0.64	7.66	8.34	-0.68	8.69	9.02	-0.33
LEF011	45.94	-90.27	11	5.93	4.28	1.65		-	*	-	-	-
LEF030	45.94	-90.27	30	8.61	11.8	-3.19	7.16	9.19	-2.03	9.73	11.53	-1.80
LEF076	45.94	-90.27	76	5.40	3.92	1.48	-	-	-	-	-	-
LEF122	45.94	-90.27	122	7.89	10.93	-3.04	6.78	8.63	-1.85	9.34	10.89	-1.55
LEF244	45.94	-90.27	244	4.51	3.49	1.02	-	-	-	-	-	-
LEF396	45.94	-90.27	396	7.71	10.59	-2.88	6.49	8.01	-1.52	8.93	10.10	-1.17
WKT009	31.32	-97.33	9	-	-	-	-	-	-	-	-	-
WKT030	31.32	-97.33	30	4.99	5.52	-0.53	5.94	6.31	-0.37	5.85	5.37	0.48
WKT061	31.32	-97.33	61	-	-	-	-	-	-	-	-	-
WKT122	31.32	-97.33	122	4.75	5.19	-0.44	5.74	5.91	-0.17	5.77	5.18	0.59
WKT244	31.32	-97.33	244	-	-	-	-	-	-	-	-	-
WKT457	31.32	-97.33	457	4.07	4.61	-0.54	5.21	5.41	-0.20	5.15	4.63	0.52
MLO	19.54	-155.58	3397	1.56	2.27	-0.71	2.33	2.63	-0.30	2.22	2.74	-0.52
BRW	71.32	-156.61	11	4.12	6.37	-2.25	3.95	5.10	-1.15	5.92	5.37	0.55
AMY	36.54	126.33	46	10.02	9.33	0.69	9.48	8.39	1.09	8.80	7.91	0.89
CDL	53.99	-105.12	600	4.96	6.53	-1.57	5.42	5.68	-0.26	-	-	-
CHM	49.69	-74.34	393	4.59	4.57	0.02	4.58	5.44	-0.86	6.17	4.08	2.09
CPT	-34.55	18.49	230	3.07	3.72	-0.65	2.64	4.56	-1.92	2.74	4.81	-2.07
FSD	49.86	-81.57	210	5.19	8.66	-3.47	5.76	7.43	-1.67	7.31	7.56	-0.25
IZO	28.31	-16.50	2373	1.98	3.12	-1.14	2.34	3.53	-1.19	3.11	3.44	-0.33
MHD	53.33	-9.90	5	-	-	-	5.11	5.78	-0.67	6.34	6.70	-0.36
NGL	53.14	15.03	62	11.89	15.73	-3.84	14.94	14.53	0.41	15.98	17.71	-1.73
RYO	39.03	141.82	260	6.03	5.45	0.58	8.41	7.23	1.18	6.75	5.86	0.89
SSL	47.90	7.92	1205	5.74	6.05	-0.31	7.83	7.88	-0.05	6.34	6.03	0.31
YON	24.47	123.01	30	3.98	3.60	0.38	5.15	3.61	1.54	5.35	3.98	1.37
ZEP	78.91	11.89	475	4.14	5.99	-1.85	3.45	4.29	-0.84	5.19	4.59	0.60

644
 645
 646 Recovered CO₂ from posterior fluxes for these sites show good agreement with the actual CO₂
 647 concentrations. Table 2 summarizes the Root Mean Square Errors (RMSE) with respect to the
 648 prior and the posterior for all the continuous sites used for the inversion. Among the prior
 649 RMSE for continuous stations, station “NGL” in Europe shows the largest average prior RMSE
 650 with 13.15 ± 1.29 ppm per year. This indicates a poor representation of the prior fluxes and/or
 651 deficiencies in the transport in that station. Very large observation errors in the station “NGL”
 652 under Section 3.1 confirms this result. Inclusion of these stations may have a significant impact
 653 on the overall solution. Posterior CO₂ concentrations at Asian stations like “RYO”, “YON”
 654 and “AMY”, show better agreement with observed CO₂ concentrations. This may be due to the
 655 effect of the CONTRAIL CO₂ measurements in the observation vector (Figure 6). Patra et al.
 656 (2008) has analyzed the synoptic-scale variability in the model simulations and observations
 657 for several approaches. This study concluded that the differences of the transport model
 658 performances depend on the horizontal and vertical characteristics of the sampling locations
 659 corresponding to each model and those are fairly independent of the size of the observed
 660 variability at the sites. In this study, it was identified that site “LEF”, which records CO₂ at
 661 several vertical layers up to about 400m, has considerably overestimated the magnitude of
 662 synoptic variations at lower levels for the period of 2002-2003. Correlations between observed
 663 and modeled CO₂ time series were also calculated and it was found that the correlation
 664 coefficient is greater than 0.3 at most stations.

665
 666
 667
 668
 669
 670

671 **Year 2009**

672

673

674

675

676

677

678

679

680

681 **Year 2010**

682

683

684

685

686

687

688

689

690

691

692

693

694

695

696

697

698

699

700

701

702

703

704

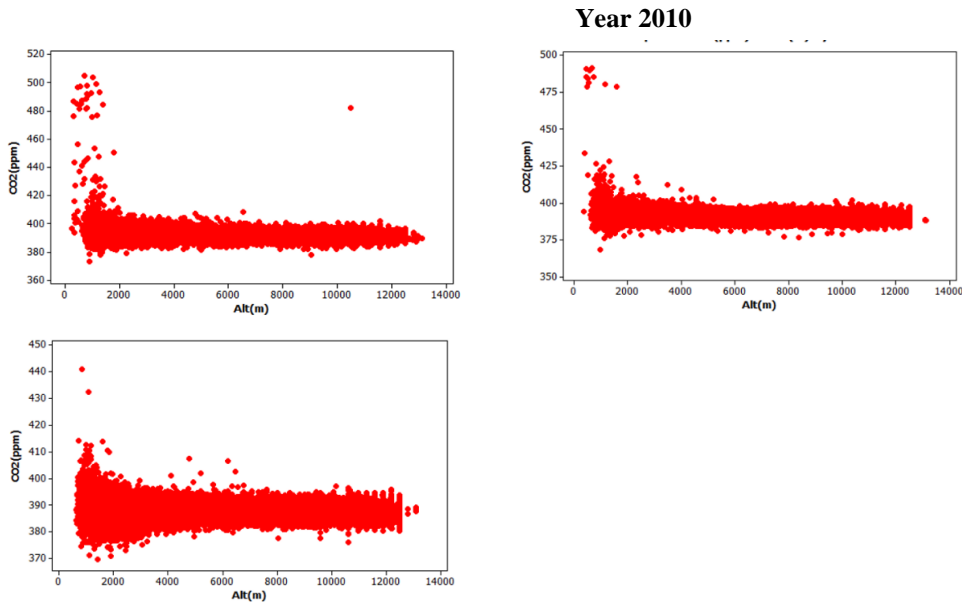


Figure 7. Variation of CONTRAIL CO₂ observations with relevant altitude (m).

Figure 7 shows the variation of the observed CONTRAIL CO₂ values with flight altitude. CONTRAIL CO₂ shows a higher variability at lower altitudes for each year. Niwa et al. (2012) also used four vertical bins as 575-625, 475-525, 375-425, 225-275 hPa because some measurements at lower altitudes (in boundary layer) are polluted by local polluted air from major cities where airports are commonly situated. They did not use the measurements below 625 hPa in order to get more accurate estimates. In this study, CONTRAIL CO₂ locations in between the altitudes from 4000m to 11000m are used for the data assimilation. The performance of MLEF method on estimating CONTRAIL aircraft data were also measured by calculating the RMSE values considering estimated posterior CO₂ and observed CO₂ values under four different height levels (i.e. 4000-5201, 5201-7074, 7074-8322 and 8322-11000 m). The RMSE values are given in Table 3.

Table 3. Root Mean Square Error (RMSE) with respect to the posterior CONTRAIL CO₂ measurements for 2009 to 2011 Units: parts per million by volume (ppmv)

		Year 2009	
Altitude in meters	Pressure level	Number of observations	RMSE (ppm)
2912 – 5202 m	350 - 625 hPa	2292	2.62
5202 – 7075 m	625 - 850 hPa	3869	2.39
7075 – 8323 m	850 - 1000 hPa	2696	2.23
8323 – 11000 m	1000 - 1325 hPa	9434	2.31

		Year 2010	
Altitude in meters	Pressure level	Number of observations	RMSE (ppm)
2912 – 5202 m	350 - 625 hPa	2128	3.11
5202 – 7075 m	625 - 850 hPa	3629	3.02
7075 – 8323 m	850 - 1000 hPa	2492	3.04
8323 – 11000 m	1000 - 1325 hPa	9668	3.14

		Year 2011	
Altitude in meters	Pressure level	Number of observations	RMSE (ppm)
2912 – 5202 m	350 - 625 hPa	2034	3.76
5202 – 7075 m	625 - 850 hPa	3359	3.74
7075 – 8323 m	850 - 1000 hPa	2313	3.64
8323 – 11000 m	1000 - 1325 hPa	8984	3.32

705

706

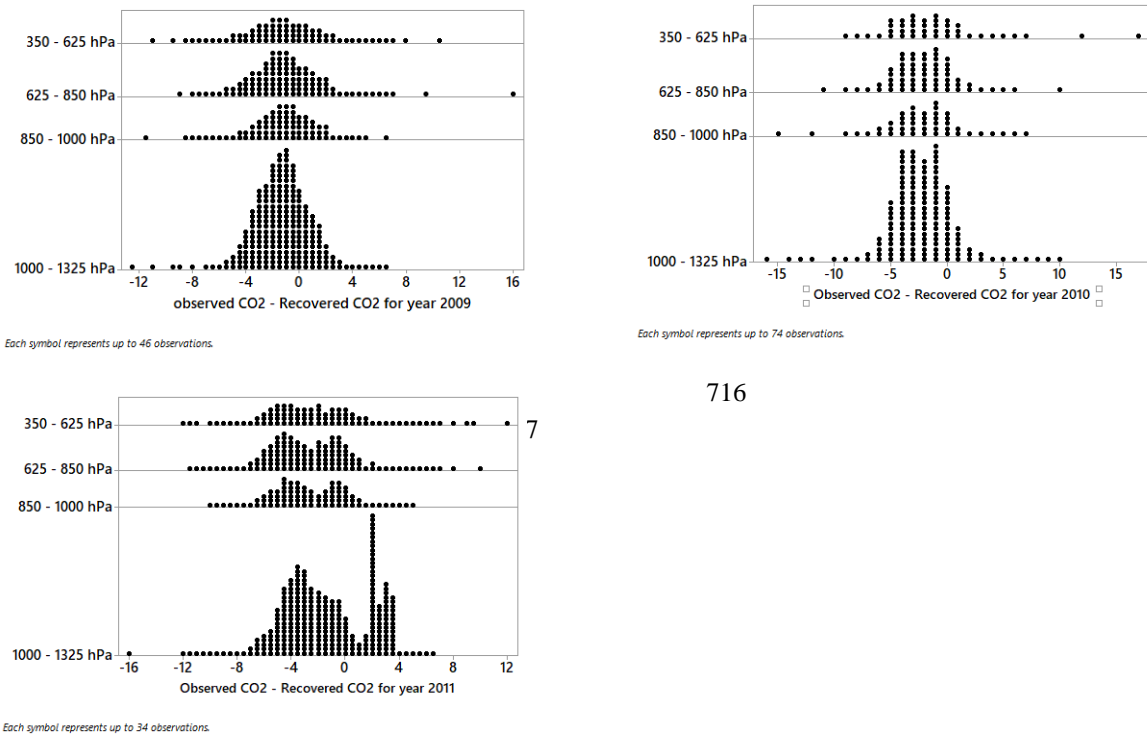
707

708

709 According to Table 3, the locations in low altitudes show relatively high RMSE values than
 710 other levels. Figure 8 shows the difference between the observed and predicted CO₂
 711 concentrations for the CONTRAIL locations under the selected altitude levels from 2009-2011.
 712 The errors are symmetrically distributed for each height level for the years 2009 and 2010
 713 except for year 2011.

714

715



716

726

727 **Figure 8.** Distribution of the difference between observed CO₂ and recovered CO₂ under four
 728 vertical bins for years 2009 to 2011.

729

730

731 3.3 Chi-square test statistic

732

733 The quality of the data assimilation process was tested using several measures. Another
 734 measure is the χ^2 statistic which evaluates the innovation (observed minus forecast
 735 observation) covariance matrix (Zupanski, 2005). Under the Gaussian assumption and for a
 736 linear observation operator, this statistic should be equal to one for statistical consistency,
 737 which suggests that the posterior uncertainty is consistent with the quality of the fit to the data.
 738 In reality, however, it is not exactly equal to one due to statistically small samples (i.e. relatively
 739 few observations per cycle). In this study, average χ^2 for the three years approximately equals
 740 0.46 ± 0.12 , 0.41 ± 0.08 and 0.42 ± 0.17 which indicates that the errors are moderately
 741 consistent.

742

743 3.4 Uncertainty reduction

744

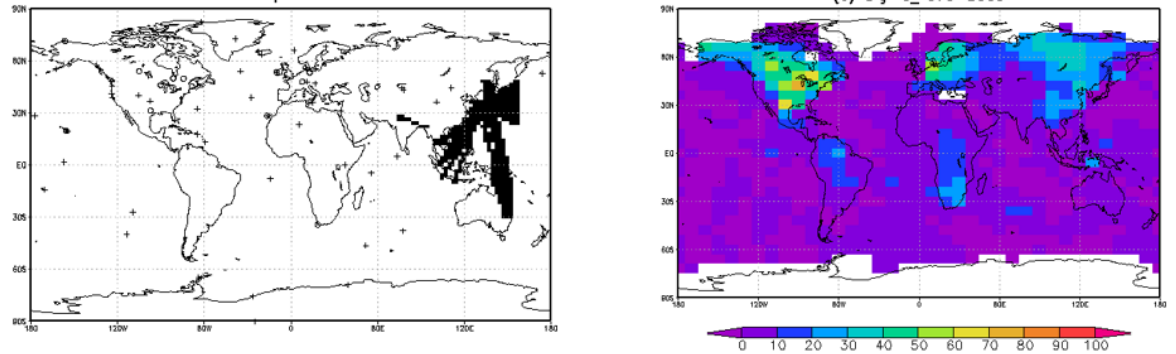
745 Figure 9 shows the average uncertainty reduction with respect to the prescribed prior
 746 uncertainty at the initial cycle. The uncertainty reduction is calculated as a percentage value as
 747 given in equation (3).

748

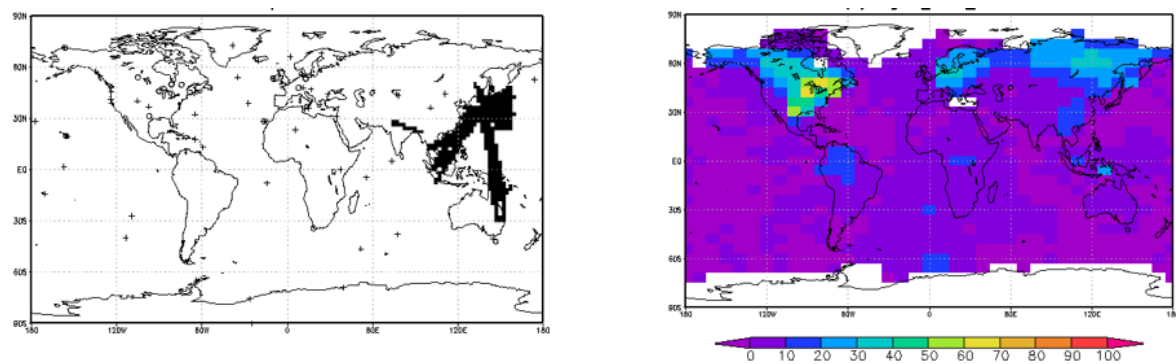
749 Uncertainty reduction = $\frac{\sigma_{prior} - \sigma_{posterior}}{\sigma_{prior}} \times 100$, (3)
 750

751 where σ_{prior} and $\sigma_{posterior}$ are the prior uncertainty at the initial cycle and the posterior
 752 uncertainty, respectively.
 753

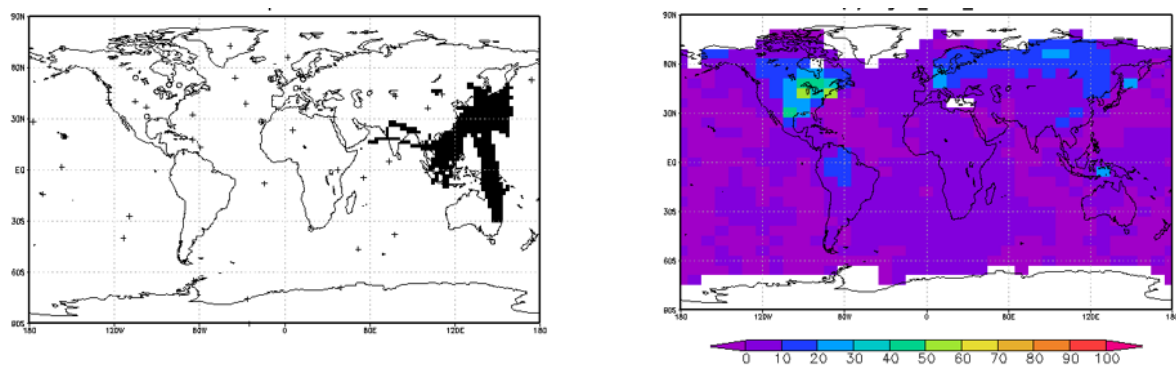
754 **(a) year 2009**



755
 756 **(b) year 2010**



757
 758 **(c) year 2011**



759
 760 **Figure 9.** Stations map with CONTRAIL locations and mean annual percentage uncertainty
 761 reduction for the years (a) 2009, (b) 2010 and (c) 2011.
 762

763
 764
 765

766 According to Figures 1 and 9 the densely observed North American region show a good
 767 constraint (about 60-80% uncertainty reduction) on flux estimates for 2009 and 60-70%
 768 reduction for 2010 and 2011. European region shows 50-60% uncertainty reduction for 2009
 769 and 40-50% reduction for 2010 and 2011. The East Asia and Southeast Asia region show about
 770 50 to 60 percent uncertainty reduction for 2009 and 30-50% reduction for 2010 and 2011. The
 771 lower uncertainty reduction in Asian region for the years 2010 and 2011 may be due to the
 772 effect of relatively high observation errors of CONTRAIL measurements in year 2010 and
 773 2011 than the year 2009 (Figure 8). The recovery of the ocean fluxes is poor due to the weak
 774 signal from the ocean flux that is observed at the stations. Ocean fluxes are an order of
 775 magnitude weaker than those on land, so the land fluxes dominate the signal (especially due to
 776 the large number of observations from continuous stations) at atmospheric observation sites on
 777 the 8-week time scale. Ocean biases are given less prior uncertainty compared to the land,
 778 which limits the uncertainty reduction in ocean fluxes. Note that we do not claim that the ocean
 779 fluxes given by the priors are correct, rather that the atmospheric observations provide
 780 insufficient constraint for our assimilation scheme to provide improved estimates at the grid
 781 scale.

782
 783 In each assimilation cycle, grid boxes that are strongly influenced by the observation network
 784 are selected according to the localization scheme and allowed to change β from the prior. Hence
 785 the posterior fluxes from sparsely observed areas are mainly dominated by the priors.
 786 Currently, grid boxes, which are selected according to the localization scheme, are equally
 787 weighted.

788
 789 The posterior land flux uncertainties have contributions from the variances of the GPP and
 790 respiration biases and their cross-covariance (see Equation 4, Lokupitiya et al., 2008).

791
 792
$$Var(F) = RESP^2 Var(\beta_{RESP}) + GPP^2 Var(\beta_{GPP}) - 2 \times RESP \times GPP \times Cov(\beta_{RESP}, \beta_{GPP})$$

 793 (4)

794
 795 We have assumed that the observation error covariance matrix (\mathbf{R}) is diagonal, which means
 796 that the observation stations are far enough from each other so that the correlations among their
 797 errors are negligible (off-diagonal elements of \mathbf{R} are zero). Inclusion of these off-diagonal
 798 covariance terms in the observation errors would produce a result that was closer to the prior
 799 (neutral carbon balance). In this study, we split the net contribution into two component fluxes,
 800 GPP and respiration. This method allows the recovery of flux patterns with a loose prior and
 801 potentially facilitates identification of each component's contribution to the NEE, which can
 802 help explain the underlying biogeochemical processes.

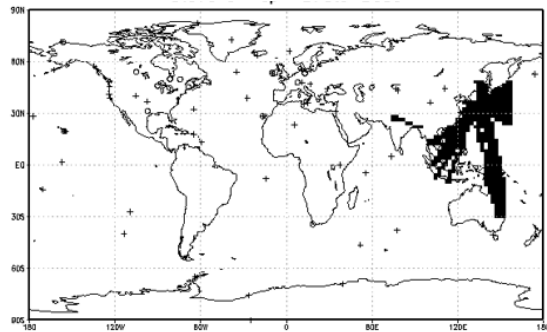
803
 804 **3.5 Comparison of optimized carbon fluxes with CT2017 fluxes**

805
 806 Fluxes optimized by MLEF are compared with the CT2017 (The version of the CarbonTracker
 807 used in this study is based on the CarbonTracker 2017 release) fluxes for the globe. The stations
 808 maps of CO₂ observation vector under the two inversion methods, MLEF and CT2017 for the
 809 period 2009-2011 are given in Figure 10. In Figure 11, left panel and the right panel show the
 810 posterior land fluxes (NEE) obtained from MLEF and CarbonTracker method (CT2017) for
 811 the years 2009-2011 respectively. CarbonTracker flux maps were created using the
 812 downloaded optimized fluxes in monthly averages from NOAA site
 813 (<http://aftp.cmdl.noaa.gov/>). The regions such as Tropical Asia, Temperate Eurasia, Australia,
 814 Europe, Boreal North America and Temperate North America were considered for the
 815 comparison due to considerable amount of observations over the region. TransCom regions in

816 southern hemisphere (SH) like South America and Africa were not considered for the
 817 comparison due to very low representation of the CO₂ observation vector over these regions.

818
 819

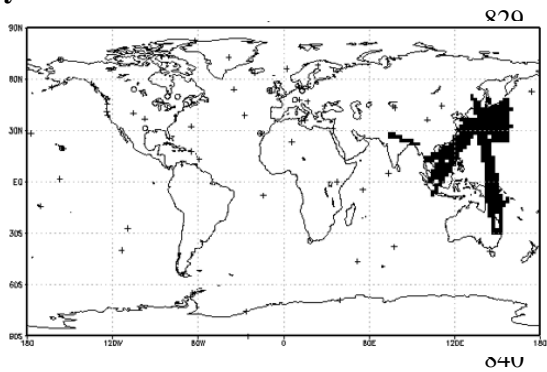
820 **Station map for MLEF**
 821 **year 2009**



822 **Open circles** – continuous sites
 823 **Crosses** – flask sampling sites
 824 **Dark squares** – CONTRAIL tracks

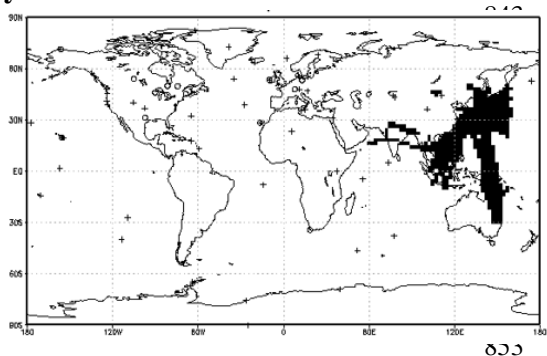
822
 823
 824
 825
 826
 827
 828

year 2010



841
 842

year 2011



854
 855
 856
 857
 858
 859

Station map for CT2017

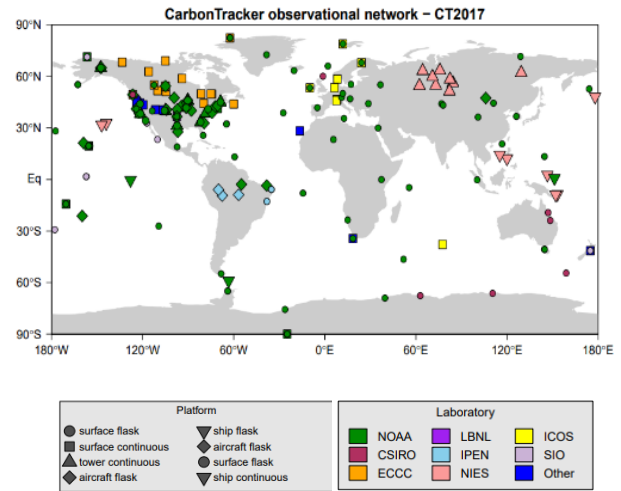
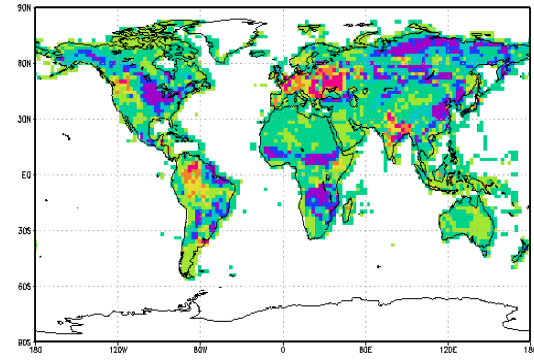
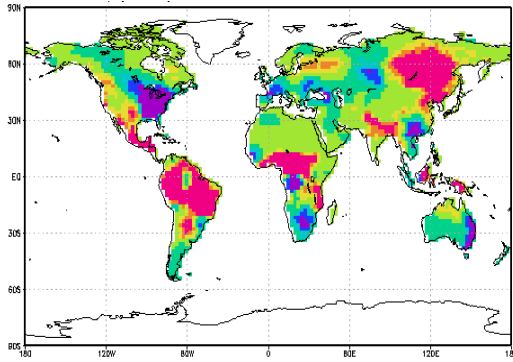


Figure 10. Stations map for MLEF (Left panel) and CT2017 (Right panel)

860

(a) MLEF - 2009

CT - 2009



861

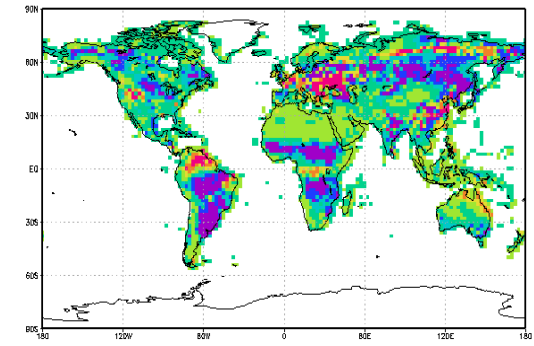
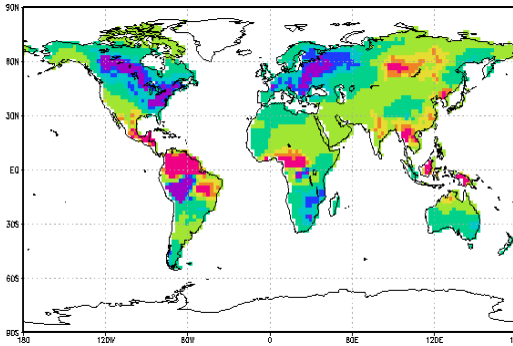
862

863

864

(b) MLEF - 2010

CT - 2010



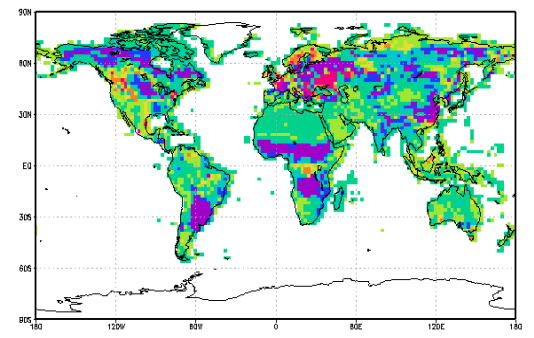
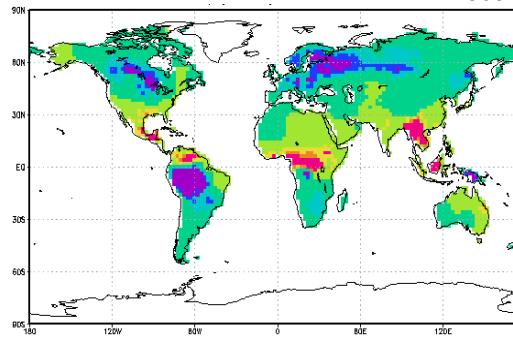
865

866

867

(c) MLEF - 2011

CT - 2011



868



869

870

871

872

873

874

875

876

877

878

879

880

881

Figure 11. Recovered Mean Annual NEE by MLEF (Left panel) and CT (CT2017) (Right panel) for the year (a) 2009, (b) 2010 and (c) 2011 respectively. Units: $\text{gC m}^{-2} \text{yr}^{-1}$.

882 According to Figure 11, spatial patterns of the estimated terrestrial biosphere fluxes for the
 883 TransCom regions show quite different results. The CO₂ observation vector used for the two
 884 inversion methods are different. This may be the reason for different spatial patterns in some
 885 regions (Figure 11). Optimized biosphere fluxes from MLEF and CarbonTracker and the prior
 886 used are summarized in Table 4 and Figure 12.

887

888 **Table 4.** Optimized surface CO₂ fluxes and their one-sigma uncertainties (PgCyr⁻¹) for the
 889 selected TransCom regions from 2009 to 2011 using MLEF and CT2017 method
 890

Region	2009		2010		2011	
	MLEF	CT	MLEF	CT	MLEF	CT
Boreal N. America	-0.004 ± 0.16	-0.30 ± 0.76	-0.427 ± 0.26	-0.37 ± 0.9	-0.27 ± 0.11	-0.62 ± 0.87
Temperate N. America	-0.476 ± 0.23	-0.50 ± 0.53	-0.296 ± 0.27	-0.3 ± 0.36	-0.045 ± 0.073	-0.05 ± 0.4
Tropical Asia	0.148 ± 0.29	-0.07 ± 0.37	0.44 ± 0.24	-0.02 ± 0.36	0.609 ± 0.146	0.07 ± 0.29
Australia	-0.142 ± 0.18	-0.04 ± 0.3	-0.002 ± 0.097	-0.01 0 ± 0.41	0.033 ± 0.047	-0.04 ± 0.33
Eurasian Temperate	0.570 ± 0.38	-0.07 ± 0.37	0.227 ± 0.17	-0.62 ± 1.55	0.096 ± 0.10	-0.97 ± 1.67
Europe	-0.036 ± 0.33	0.37 ± 1.77	-0.662 ± 0.35	0.08 ± 2.12	-0.576 ± 0.194	-0.17 ± 1.89
Land Total	5.648	-3.33 ± 4.19	0.741	4.55 ± 4.03	-1.169	-4.91 ± 3.97
Ocean Total	-1.430	-3.13 ± 1.45	-1.448	-2.26 ± 1.40	-1.511	-2.80 ± 1.07

891
 892
 893
 894
 895
 896
 897
 898
 899
 900
 901
 902
 903
 904
 905
 906
 907
 908
 909
 910
 911

912
913
914
915
916
917
918
919
920
921
922
923
924
925
926
927
928
929
930
931
932
933
934
935
936
937
938
939
940
941
942
943
944
945
946
947
948
949
950
951
952
953
954
955
956
957
958
959
960
961
962

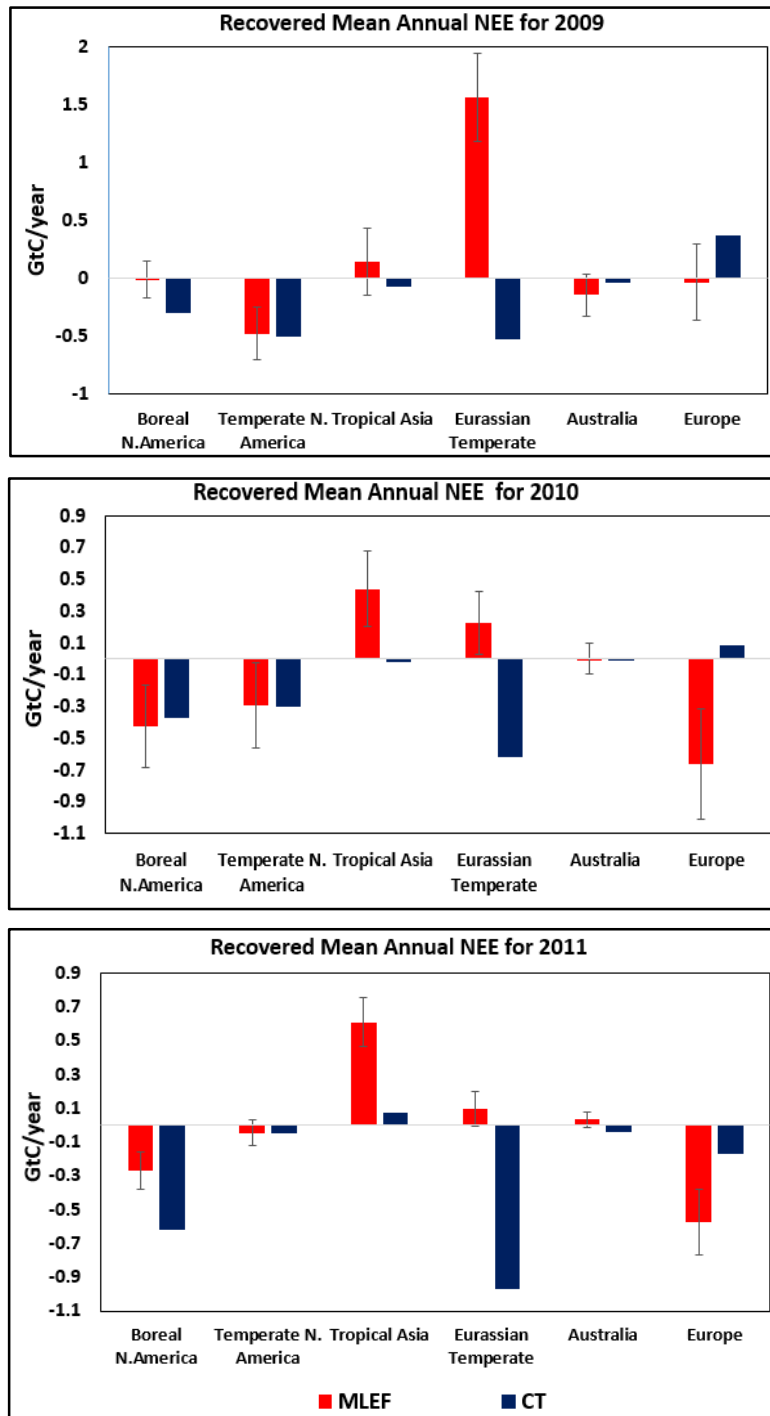


Figure 12. Mean annual NEE with 1- σ error bars aggregated to TransCom regions; Boreal North America, Temperate North America, Europe, Tropical Asia, Eurasian Temperate and Australia, estimated by MLEF and CarbonTracker (a) for 2009, (b) for 2010 and (c) for 2011. Units: GtC/year.

Spatial distribution of the mean annual CO₂ land fluxes derived from MLEF over North American region and several parts of the Asian region, like South Asia and Southeast Asia show good agreement with the CarbonTracker fluxes. South Asian region seems to be carbon

963 neutral for year 2011 and the observed carbon source pattern under CarbonTracker for year
964 2009 was also well captured by our model (Figure 11). Boreal North America and Temperate
965 North America are highly rich in surface flask and continuous CO₂ measurement sites and those
966 are carbon sinks with MLEF results, for the years from 2009-2011. This result shows good
967 agreement with the CarbonTracker fluxes (Figure 11, 12). MLEF fluxes show that the Tropical
968 Asia is a carbon source. But it is a weak sink for the years 2009 and 2010 and is a source for
969 year 2011 under the CarbonTracker results. In our study, the selected CONTRAIL aircraft
970 tracks mainly cover the regions of South Asia, Southeast Asia, East Asia and Australia (Figure
971 10). But, those regions are poorly represented in flask and continuous CO₂ measurement sites
972 (see Figure 1). In CT2017, optimized fluxes for the above regions have the effect of densely
973 available flask and continuous sampling sites than what we have used in MLEF method. This
974 may be the reason for the difference between the optimized flux in Tropical Asia.

975

976 In Eurasian Temperate region, our optimized land fluxes for the period 2009-2011 (on average
977 it is +0.53 PgCyr⁻¹) is different from CarbonTracker results (Figure 12) which shows it as a
978 carbon sink. The reason for this difference may be the impact of the atmospheric CO₂
979 observation network we used. There are several flask and continuous observation sites covering
980 the East Asia in CT2017 (Figure 10) than MLEF. In this study, Europe is a carbon sink for the
981 years 2009-2011. According to CarbonTracker results it is a carbon source for the years 2009
982 and 2010 and a carbon sink for year 2011 (Figure 11). This difference may due to the effect of
983 densely observed surface continuous CO₂ sites used in CT2017 rather than MLEF data
984 assimilation (Figure 10).

985

986 MLEF solves for biases at the grid-scale and does not impose any prior spatial patterns into the
987 fluxes (recall that the prior annual NEE in SiB is identically zero at every grid cell). Biomass
988 emissions are not included in SiB priors. However, CarbonTracker solves for fluxes by
989 prescribing spatial patterns according to eco-regions (Peters et al., 2005; 2007). The large basis
990 regions used in CarbonTracker is beneficial in recovering fluxes over sparsely sampled regions;
991 however, it restricts changes to the prescribed spatial flux patterns even in densely observed
992 areas. However, the spatial distribution of the mean annual fluxes over North America,
993 Australia and several regions in Asia derived from the MLEF and CarbonTracker show similar
994 results when aggregated into large (TransCom) regions.

995

996

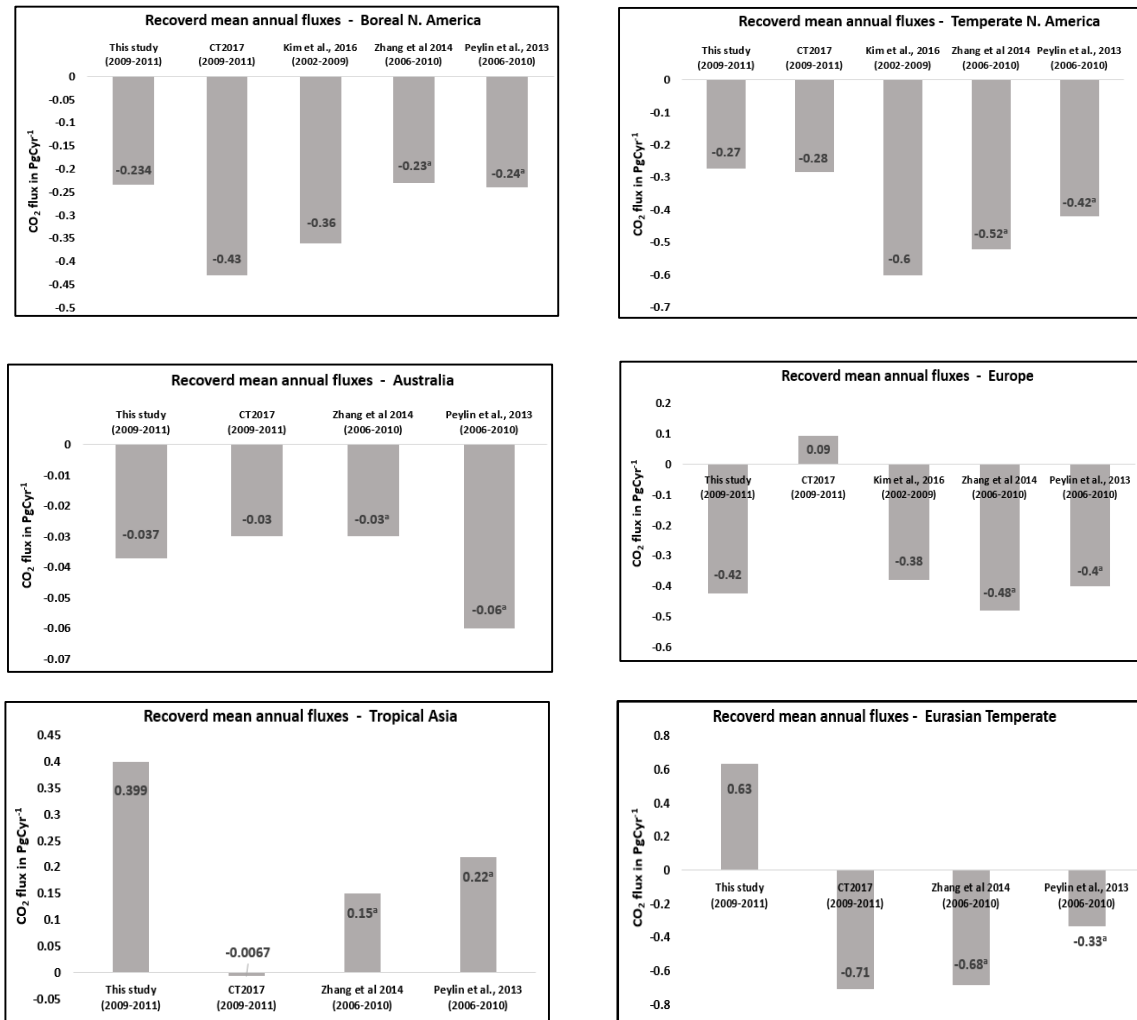
997 **3.6 Comparison of optimized carbon fluxes with other studies**

998

999 Comparison of the MLEF optimized CO₂ fluxes with other inverse modelling methods for the
1000 selected TransCom regions are summarized in Figure 13. MLEF results are mainly compared
1001 with the results of CT2017, Kim et al. (2017), Peylin et al. (2013) and Zhang et al. (2014) by
1002 considering the time period and the CO₂ observation network used for the optimization. Zhang
1003 et al. (2014) used CarbonTracker data assimilation method with surface and CONTRAIL
1004 measurements to obtain optimized fluxes for the years 2006-2010. Peylin et al. (2013) also
1005 used CarbonTracker method using flask and continuous CO₂ observations and obtained
1006 optimized carbon fluxes for TransCom regions for the years 2006-2010. The optimized fluxes
1007 by Peylin et al. (2013) were obtained from the online supplement (available online at
1008 <http://www.biogeosciences.net/10/6699/2013/bg-10-6699-2013-supplement.pdf>). Kim et al.
1009 (2017) also used CarbonTracker method to estimate carbon fluxes for the TransCom regions
1010 using Siberian observations during the years 2002-2009. In the next step, the spatial distribution
1011 of the optimized CO₂ fluxes in South Asian (which includes the countries Bangladesh, Bhutan,
1012 India, Nepal, Pakistan and Sri Lanka) region was compared with MLEF results considering

1013 several studies in the literature (Patra et al., 2013, Jiang et al., 2014, and Thompson et al.,
 1014 2016). Finally, the MLEF results obtained by assimilating surface and CONTRAIL CO₂
 1015 observations are compared with the results of inverse modelling studies which used surface
 1016 and Greenhouse Gases Observing Satellite (GOSAT) total column CO₂ (XCO₂) observations
 1017 for their flux inversion.

1018
 1019



1020
 1021
 1022
 1023
 1024
 1025
 1026
 1027

Figure 13. Comparison of optimized surface CO₂ fluxes (GtC yr⁻¹) from MLEF with other studies

^aBiomass burning emissions are included into the land fluxes

1028 Optimized carbon fluxes in other studies are summarized with MLEF optimized land fluxes
 1029 and are given in Figure 13 (Note: In Zhang et al. (2014) and Peylin et al. (2013), the optimized
 1030 fluxes include land and fire emissions). The average annual recovered fluxes from MLEF for
 1031 Boreal North America (-0.234 PgCyr⁻¹), Temperate North America (-0.27 PgCyr⁻¹), Australia
 1032 (-0.037 PgCyr⁻¹) and Europe (-0.42 PgCyr⁻¹) during the period from 2006-2010 (carbon sinks)
 1033 are more comparable with the estimated fluxes in other selected studies.

1034 According to Zhang et al. (2014), mean terrestrial carbon uptake in Asia is -1.56 (= land fluxes
 1035 + fire emissions) PgCyr^{-1} which was further partitioned into -1.02 PgCyr^{-1} carbon sink in Boreal
 1036 Eurasia and -0.68 PgCyr^{-1} carbon sink in Temperate Eurasia and a $+0.15$ PgCyr^{-1} CO_2 source
 1037 in Tropical Asia. Zhang et al. (2014) shows that posterior land flux for the Tropical Asia is $-$
 1038 0.17 ± 0.28 PgCyr^{-1} from 2006-2010. According to the MLEF results, Tropical Asia is a carbon
 1039 source ($+0.399$ PgCyr^{-1}) from 2009-2011. Other than that, CT2017 also shows a weak sink ($-$
 1040 0.0067 PgCyr^{-1}) for this region. The number of CONTRAIL-JAL aircraft tracks used in our
 1041 study (from year 2009–2011) shows more coverage than the CONTRAIL used in Zhang et al.
 1042 (2014) over Tropical Asian region (see Figure 10 and Figure 1. (b) in Zhang et al., 2014). This
 1043 may be the reason for this difference in Tropical Asian flux estimates. MLEF results show that
 1044 the Eurasian Temperate is a carbon source ($+0.63$ PgCyr^{-1}) and this results is not compatible
 1045 with other studies. The discrepancy between the results in Temperate Eurasia may be due to
 1046 the CO_2 observation network used. Zhang et al. (2014), has more coverage of CONTRAIL
 1047 observations over Boreal Eurasia to Europe (Figure 1. (b) in Zhang et al., 2014) rather than the
 1048 CONTRAIL CO_2 we used in our study. The CO_2 observation network used by Peylin et al.
 1049 (2013) is the same as the CarbonTracker and it has more coverage of flask and continuous sites
 1050 in Boreal and Temperate Eurasian regions. These observation networks reveal an insufficient
 1051 observation coverage in this region and it may have an effect on the estimated land fluxes in
 1052 Eurasian Temperate region. Finally, as an overall result, it can be said that the MLEF results
 1053 with surface and CONTRAIL CO_2 observations show reasonable estimates for the selected
 1054 TransCom regions when compared with the results of the studies discussed above.

1055
 1056 Patra et al. (2013) has presented the net carbon budget for the South Asia for the period 1990-
 1057 2009. Based on the atmospheric CO_2 inversions, it was found that net biospheric CO_2 flux in
 1058 South Asia was a sink ($-104 \pm 150 \text{TgC yr}^{-1}$) during the period of 2007-2008. Jiang et al. (2014)
 1059 estimated terrestrial CO_2 flux in China during 2002-2008 using an atmospheric inversion
 1060 method with passenger aircraft-based CO_2 measurements over Eurasia. The results showed that
 1061 with the addition of CONRATL CO_2 data, it increased the carbon sink in China from $-$
 1062 0.16 ± 0.19 to -0.29 ± 0.18 PgCyr^{-1} while decreasing the carbon sink in Southeast and South Asia
 1063 by -0.68 ± 0.34 to -0.28 ± 0.32 and -0.35 ± 0.30 to -0.11 ± 0.30 PgCyr^{-1} , respectively. Thompson et
 1064 al. (2016) assessed the carbon budget of Asia under seven atmospheric CO_2 inversions focusing
 1065 East, South and Southeast Asian regions. According to the results from the inversion ensemble,
 1066 Thompson et al. (2016) found that the land biosphere in South Asia was close to being carbon
 1067 neutral with a flux of -0.05 (-0.18 to 0.03) PgC per year for the period 1996-2012. The surface
 1068 carbon flux for South Asian region was not quantified in this study. But, the spatial distribution
 1069 of the MLEF carbon flux in South Asian region shows more compatible results with the
 1070 CT2017 results (Figure 11) and other selected studies.

1071
 1072 Saeki et al. (2013) conducted an inverse modelling analysis to estimate the surface carbon flux
 1073 using column-averaged dry air mole fractions of CO_2 observed by the GOSAT (which started
 1074 to record observations from year 2009) and ground based data from June 2009 to October 2010.
 1075 The results showed that the annual total sink for the South Asian region (June 2009-May 2010)
 1076 was 0.23 PgC yr^{-1} from NOAA data inversion, while NOAA plus GOSAT gave a stronger sink
 1077 of 0.48 PgC yr^{-1} . GOSAT XCO_2 contains information about the free and upper troposphere like
 1078 CONTRAIL CO_2 measurements (Basu et al., 2014). Basu et al. (2014), estimated CO_2 flux
 1079 over Tropical Asia in 2009, 2010 and 2011 using RemoTec v2.11 retrievals of GOSAT XCO_2
 1080 and surface measurements of CO_2 , using four-dimensional variational (4DVAR) atmospheric
 1081 inversion using the atmospheric tracer transport model TM5. According to the surface CO_2
 1082 flux per 3 month time window obtained (Basu et al., 2014-Figure 2), Tropical Asia seems to
 1083 be a source from GOSAT estimates. This results is more compatible with MLEF result for

1084 Tropical Asia which is a carbon source (Figure 12). According to Basu et al. (2014), this
 1085 increased source estimate is consistent with CONTRAIL measurements. Basu et al. (2013),
 1086 optimized global source-sink estimates using surface and GOSAT CO₂ data from 1st September
 1087 2009 to 1st September 2010 and the results can be compared with MLEF results with surface
 1088 and CONTRAIL observations. According to Basu et al. (2013), North American prior source
 1089 (0.4 ± 0.5 PgC) converted to a posterior sink (0.4 ± 0.20 PgC) using surface data and this sink
 1090 was strengthened by 1.0 ± 1.0 PgC using surface and GOSAT data. Prior source (0.3 ± 0.40
 1091 PgC) of the Europe, converted to a sink (0.3 ± 0.30 PgC) by surface data and with addition of
 1092 GOSAT strengthened the sink by 1.3 ± 0.20 PgC. Eurasian temperate region is a sink (0.1 ± 0.20
 1093 PgC) with surface data and it was a source (0.3 ± 0.20 PgC) with both measurements. Prior
 1094 source (0.3 ± 0.7 PgC) for the tropics is increased by surface data to 0.5 ± 0.4 PgC and it was
 1095 further increased to 2.1 ± 0.20 PgC by adding GOSAT. Estimated posterior for North America,
 1096 Europe and Eurasian Temperate with surface and GOSAT data in Basu et al. (2013) are
 1097 comparable with the posterior fluxes estimated using surface and CONTRAIL data using
 1098 MLEF (Figure 12).

1099 **4 Conclusions**

1100 This paper presents the first application of the MLEF method to assimilate existing flasks,
 1101 continuous observations and CONTRAIL measurements. Previously, this assimilation system
 1102 was tested with a pseudo-data experiment, which showed satisfactory results over the densely
 1103 observed areas (Lokupitiya et al., 2008; Perera et al., 2017). In this study, flux estimation is
 1104 done by separating NEE into GPP and respiration components and hence is potentially useful
 1105 in identifying the driving forces of the carbon sinks. Currently, however, the daytime
 1106 atmospheric CO₂ observations that we assimilate cannot be adequately separated into these two
 1107 components. Nighttime CO₂ observations contain information about respiration, but the
 1108 transport models poorly represent the nighttime values. In order to separate these components,
 1109 additional constraints could be added to the model, such as carbonyl sulfide as a tracer of GPP
 1110 (Lokupitiya et al., 2008).

1111
 1112 In this paper, we have given flux estimates for densely observed North America, Europe and
 1113 Asia, where we expect the observation network to provide additional constraints for years
 1114 2009-2011. A comparison of the results with another similar technique, CarbonTracker
 1115 (CT2017), shows good agreement at large (TransCom) regional scale. However, spatial
 1116 patterns are quite different, which seem to be dominated by the differences in prior
 1117 assumptions, especially the hard constraint of ecosystem classification used to scale net fluxes
 1118 in CarbonTracker. The grid scale inversion setup that we considered here can produce
 1119 satisfactory annual mean flux estimates over the densely observed regions. However, the
 1120 recovered fluxes at grid scale over sparsely sampled regions are not reliable. The method
 1121 recovers fluxes in North America, Asia and Europe with less uncertainty. North America shows
 1122 about 60-80% uncertainty reduction. Moderate results are obtained over the Asian and
 1123 European region with about 50-60% uncertainty reduction. Most other land and oceanic regions
 1124 show less than 30% uncertainty reduction. Recovery from the oceanic regions has high
 1125 uncertainties because currently available atmospheric observations poorly constrain the weaker
 1126 oceanic fluxes.

1127
 1128 MLEF results with surface and CONTRAIL CO₂ observation network are more similar with
 1129 other studies which used surface observations, surface plus CONTRAIL observations, surface
 1130 plus Siberian observations and surface plus GOSAT observations in the CO₂ observation
 1131 vector. Optimized fluxes in Temperate North America, Boreal North America, Australia,
 1132 Europe and Tropical Asia are comparable with optimized fluxes with other studies. However,

1133 we found several discrepancies in the spatial distribution of the optimized fluxes and estimated
1134 flux for some TransCom regions. In flux inversions, the optimized fluxes mainly depend on
1135 several factors such as prior guess, transport model used, CO₂ observation network, etc. These
1136 may be the main reasons for the above incompatibilities.

1137

1138 The main conclusion that can be drawn from this study is that grid scale inversions can produce
1139 satisfactory regional results when aggregated into larger regions, given the regions are densely
1140 observed in space and time. Fluxes in more sparsely observed regions in southern hemisphere
1141 like Africa and South America were poorly recovered from the MLEF method. The
1142 decomposition of net terrestrial fluxes into gross fluxes driven by well understood fast
1143 processes and the focus of statistical power from the observations on the poorly understood
1144 slow biogeochemistry allow the regional flux estimation from current networks without the
1145 need for hard constraints in the form of ecosystem maps or assumed covariance structures used
1146 in previous studies.

1147

1148 MLEF performs well with high dimensional observation vectors and does not require
1149 computationally intensive sequential assimilation schemes. Hence, it is more suitable for
1150 assimilation of satellite retrievals. As networks of continuous observing sites, aircraft sampling,
1151 and satellite observing systems will emerge in the coming years, this framework can be easily
1152 extensible to those much larger data vectors. In a future paper, this assimilation system will be
1153 used to assimilate satellite observations from GOSAT and/or OCO₂ projects.

1154 **Acknowledgments**

1155 This research is supported by the grants from NRC-Sri Lanka (National Research Council, Sri
1156 Lanka) (NRC-036) and APN (Asia-Pacific Network for Global Change Research;
1157 grant#ARCP2011-11NMY-Patra/Canadell). We gratefully acknowledge the computer support
1158 provided by Matt Bishop, Department of Atmospheric Science, Colorado State University, Fort
1159 Collins, Colorado, USA, Harsha Munasingha and Suresh Nanayakkara, Centre for IT Services,
1160 University of Sri Jayewardenepura, Sri Lanka and Nuwan De Silva, Softlogic IT, Sri Lanka.
1161 CO₂ measurements used in this study are available from World Data Center for Greenhouse
1162 Gases (<http://gaw.kishou.go.jp/>) and the ObsPack data product
1163 (<https://www.esrl.noaa.gov/gmd/ccgg/obspack/>). We kindly acknowledge all atmospheric data
1164 providers to the GMD (Global Monitoring Division) data archive, NOAA/ESRL and those that
1165 contribute their data to WDCGG site and the CONTRAIL PIs Toshinobu Machida, Hidekazu
1166 Matsueda, Yousuke Sawa and Yosuke Niwa. We appreciate the CarbonTracker 2017 results
1167 obtained by NOAA ESRL, Boulder, Colorado, USA from the website
1168 (<http://carbontracker.noaa.gov/>) and MERRA-2 weather data downloaded from
1169 <https://disc.gsfc.nasa.gov/>, managed by the NASA Goddard Earth Sciences (GES) Data and
1170 Information Services Center (DISC) for our study.

1171

1172 **References**

- 1173 Al-Ghussain, L. (2018). Global Warming: Review on Driving Forces and Mitigation.
1174 *Environmental Progress & Sustainable Energy*, 38(1), 13-21. <https://doi.org/10.1002/ep>
1175
- 1176 Baker, I., Denning, A. S., Hanan, N., Prihodko, L., Uliasz, M., Vidale, P. L., Daviss, K., &
1177 Bakwin, P. (2003). Simulated and observed fluxes of sensible and latent heat and CO₂ at the
1178 WLEF-TV Tower using SiB2.5. *Global Change Biology*, 9, 1262-1277.
1179 <https://doi.org/10.1046/j.1365-2486.2003.00671.x>

- 1180 Baker, D. F., Doney, S. C., & Schimel, D. S. (2006). Variational data assimilation for
 1181 atmospheric CO₂. *Tellus (2006)*, 58B, 359-365. [https://doi: 10.1111/j.1600-0889.2006.00218.x](https://doi:10.1111/j.1600-0889.2006.00218.x)
 1182
- 1183 Basu, S., Guerlet, S., Butz, A., Houweling, S., Hasekamp, O., Aben, I., Krummel, P., Steele,
 1184 P., Langenfelds, R., Torn, M., Biraud, S., Stephens, B., Andrews, A., & Worthy, D. (2013).
 1185 Global CO₂ fluxes estimated from GOSAT retrievals of total columnCO₂. *Atmos. Chem. Phys.*,
 1186 13, 8695–8717. <https://doi:10.5194/acp-13-8695-2013>.
 1187
- 1188 Basu, S., Krol, M., Butz, A., Clerbaux, C., Sawa, Y., Machida, T., Matsueda, H., Frankenberg,
 1189 C., Hasekamp, O. P., & Aben, I. (2014). The seasonal variation of the CO₂ flux over Tropical
 1190 Asia estimated from GOSAT, CONTRAIL, and IASI. *Geophys. Res. Lett.*, 41, 1809–1815,
 1191 doi:10.1002/2013GL059105
 1192
- 1193 Brenkert, A. (1998). Carbon dioxide emission estimates from fossil-fuel burning, hydraulic
 1194 cement production, and gas flaring for 1995 on a one-degree grid cell basis. *Tech Rep NDP-*
 1195 *058A*, Carbon Dioxide Information Analysis Center, Oak Ridge Natl. Lab., Oak Ridge, Tenn.
 1196 (Available at <http://cdiac.ess-dive.lbl.gov/newsletr/fall98/ccf98.pdf>).
 1197
- 1198 Bruhwiler, L. M. P., Michalak, A. M., Peters, W., Baker, D. F., & Tans, P. (2005). An improved
 1199 Kalman Smoother for atmospheric inversions. *Atmospheric Chemistry and Physics*, 5, 2691-
 1200 2702. <https://doi.org/10.5194/acp-5-2691-2005>
 1201
- 1202 Bosilovich, M. G., Lucchesi, R., & Suarez, M. (2016). *MERRA-2: File Specification*. GMAO
 1203 Office Note No. 9 (Version 1.1), 73 pp, available from
 1204 http://gmao.gsfc.nasa.gov/pubs/office_notes.
 1205
- 1206 *CarbonTracker CT2017*. Retrieved from
 1207 <https://www.esrl.noaa.gov/gmd/ccgg/carbontracker/CT2017/>.
 1208
- 1209 Chatterjee, A. (2012). *Data Assimilation for Atmospheric CO₂: Towards Improved Estimates*
 1210 *of CO₂ Concentrations and Fluxes*, (Doctoral Dissertation, University of Michigan). Retrieved
 1211 from Deep Blue. (<https://deepblue.lib.umich.edu/handle/2027.42/96172>).
 1212
- 1213 Chatterjee, A., Michalak, A. M., Anderson, J. L., Mueller, K. L., & Yadav, V. (2012). Toward
 1214 reliable ensemble Kalman filter estimates of CO₂ fluxes. *Journal of Geophysical Research*,
 1215 117, D22306. <https://doi:10.1029/2012JD018176>
 1216
- 1217 Chevallier F., Fisher M., Peylin P., Serrar S., Bousquet P., Bre´on, F.-M., Che´din A., & Ciais
 1218 P. (2005). Inferring CO₂ sources and sinks from satellite observations: Method and application
 1219 to TOVS data. *Journal of Geophysical Research*, 110, D24309.
 1220 <https://doi:10.1029/2005JD006390>.
 1221
- 1222 *GLOBALVIEW-CO₂*. Retrieved from <https://www.esrl.noaa.gov/gmd/ccgg/obspack/>.
 1223
- 1224 Gurney, K. R., Law, R. M., Denning, A. S., Rayner, P. J., Baker, D., Bousquet, P.,
 1225 Bruhwiler, L., Chen, Ciais, Y. H., P., Fan, S., Fung, I. Y., Gloor, M., Heimann, M.,
 1226 Higuchi, K., John, J., Maki, T., Maksyutov, S., Masarie, K., Peylin, P., Prather, M., Pak,
 1227 B. C., Randerson, J., Sarmiento, J., Taguchi, S., Takahashi, T., & Yuen, C. W. (2002).
 1228 Towards robust regional estimates of CO₂ sources and sinks using atmospheric transport
 1229 models. *Nature*, 415, 626-630.

- 1230 Feng, L., Palmer, P. I., Bösch, H., & Dance, S. (2009). Estimating surface CO₂ fluxes from
 1231 space-borne CO₂ dry air mole fraction observations using an ensemble Kalman Filter. *Atmos.*
 1232 *Chem. Phys.*, 9, 2619–2633. <https://doi.org/10.5194/acp-9-2619-2009>
 1233
- 1234 Jiang F., Wang, H. W., Chen, J. M., Zhou, L. X., Ju, W. M., Ding, A. J., Liu, L. X., & Peters,
 1235 W. (2013). Nested atmospheric inversion for the terrestrial carbon sources and sinks in China.
 1236 *Biogeosciences*, 10, 5311–5324. <https://doi:10.5194/bg-10-5311-2013>
 1237
- 1238 Jiang, F., Wang, H. M., Chen, J. M., Machida, T., Zhou, L. X., Ju, W. M., Matsueda, H.,
 1239 & Sawa, Y. (2014). Carbon balance of China constrained by CONTRAIL aircraft CO₂
 1240 measurements. *Atmos. Chem. Phys.*, 14, 10133–10144. [https://doi:10.5194/acp-14-10133-](https://doi:10.5194/acp-14-10133-2014)
 1241 2014
 1242
- 1243 Kaminski, T., Rayner, P. J., Heimann, M., & Entin, I. G. (2001). On aggregation errors in
 1244 atmospheric transport inversions. *Journal of Geophysical Research*, 106, 4703–
 1245 4715. <https://doi.org/10.1029/2000JD900581>
 1246
- 1247 Kang, J. S., Kalnay, E., Liu, J., Fung, I., Miyoshi, T., & Ide, K. (2011). “Variable
 1248 localization” in an ensemble Kalman filter: Application to the carbon cycle data
 1249 assimilation. *Journal of Geophysical Research*, 116, D09110.
 1250 <https://doi:10.1029/2010JD014673>
 1251
- 1252 Kawa, S. R., Erickson III, D. J., Pawson, S., & Zhu, Z. (2004). Global CO₂ transport
 1253 simulations using meteorological data from the NASA data assimilation system. *Journal*
 1254 *of Geophysical Research*, 109, D18312, <https://doi:10.1029/2004JD004554>.
 1255
- 1256 Kim, J., Kim, H. M., & Cho, C., (2014). Influence of CO₂ observations on the optimized
 1257 CO₂ flux in an ensemble Kalman filter. *Atmos. Chem. Phys.*, 14, 13515–13530.
 1258 <https://doi.org/10.5194/acp-14-13515-2014>
 1259
- 1260 Kim, J., Kim, H. M., Cho, C., Boo, K., Jacobson, A. R., Sasakawa, M., Machida, T., Arshinov,
 1261 M., & Fedoseev, N., (2017). Impact of Siberian observations on the optimization of surface
 1262 CO₂ flux. *Atmos. Chem. Phys.*, 17, 2881–2899. <http://doi:10.5194/acp-17-2881-2017>
 1263
- 1264 Kondo, M., Patra, P.K., Sitch, S., Friedlingstein, P., Poulter, B., Chevallier, F., Ciais, P.,
 1265 Canadell, J. G., Bastos, A., Lauerwald, R., Calle, L., Ichii, K., Anthoni, P., Arneth, A., Haverd,
 1266 V., Jain, A. K., Kato, E., Kautz, M., Law, R.M., Lienert, S., Lombardozzi, D., Maki, T.,
 1267 Nakamura, T., Peylin, P., Rödenbeck, C., Zhuravlev, R., Saeki, T., Tian, H., Zhu, D., & Ziehn,
 1268 T. (2019). State of the science in reconciling top-down and bottom-up approaches for terrestrial
 1269 CO₂ budget, *Glob Change Biology*, 1-17. <https://doi:10.1111/gcb.14917>
 1270
- 1271 Le Quéré, C., Andrew, R. M., Friedlingstein, P., Sitch, S., Hauck, J., Pongratz, J., Pickers, P.
 1272 A., Korsbakken, J. I., Peters, G. P., Canadell, J. G., Arneth, A., Arora, V. K., Barbero, L.,
 1273 Bastos, A., Bopp, L., Chevallier, F., Chini, L. P., Ciais, P., Doney, S. C., Gkritzalis, T., Goll,
 1274 D. S., Harris, I., Haverd, V., Hoffman, F. M., Hoppema, M., Houghton, R. A., Hurtt, G., Ilyina,
 1275 T., Jain, A. K., Johannessen, T., Jones, C. D., Kato, E., Keeling, R. F., Goldewijk, K. K.,
 1276 Landschützer, P., Lefèvre, N., Lienert, S., Liu, Z., Lombardozzi, D., Metzl, N., Munro, D. R.,
 1277 Nabel, J. E. M. S., Nakaoka, Shin-ichiro., Neill, C., Olsen, A., Ono, T., Patra, P., Pregon, A.,
 1278 Peters, W., Peylin, P., Pfeil, B., Pierrot, D., Poulter, B., Rehder, G., Resplandy, L., Robertson,
 1279 E., Rocher, M., Rödenbeck, C., Schuster, U., Schwinger, J., Séférian, R., Skjelvan, I.,

- 1280 Steinhoff, T., Sutton, A., Tans, P. P., Tian, H., Tilbrook, B., Tubiello, F. N., Laan-Luijkx,
 1281 Ingrid T. van der., Werf, Guido R. van der., Viovy, N., Walker, A. P., Wiltshire, A. J., Wright,
 1282 R., Zaehle, S., & Zheng, B. (2018). Global Carbon Budget 2018. *Earth Syst. Sci. Data*, 10,
 1283 2141–2194. <https://doi.org/10.5194/essd-10-2141-2018>
 1284
- 1285 Lokupitiya, R. S., Zupanski, D., Denning, A. S. Kawa, S. R., Gurney, K. R., & Zupanski,
 1286 M. (2008). Estimation of global CO₂ fluxes at regional scale using the maximum likelihood
 1287 ensemble filter. *Journal of Geophysical Research*. 113, D20110.
 1288 <http://doi:10.1029/2007JD009679>.
 1289
- 1290 Michalak, A. M., Bruhwiler, L., & Tans, P. P. (2004). A geostatistical approach to surface
 1291 flux estimation of atmospheric trace gases. *Journal of Geophysical Research*. 109,
 1292 D14109. <https://doi:10.1029/2003JD004422>.
 1293
- 1294 Miyazaki, K., Maki, T., Prabir, P., & Nakazawa, T. (2011), Assessing the impact of satellite,
 1295 aircraft, and surface observations on CO₂ flux estimation using an ensemble-based 4-D data
 1296 assimilation system. *Journal of Geophysical Research*, 116. D16306.
 1297 <https://doi:10.1029/2010JD015366>
 1298
- 1299 Machida, T., Matuseda, H., Sawa, Y., Nakagawa, Y., Hirokani, K., Kondo, N., Goto, K.,
 1300 Nakazawa, T., Ishikawa, K., Ogawa, T. (2008). Worldwide Measurements of Atmospheric
 1301 CO₂ and Other Trace Gas Species Using Commercial Airlines. *Journal of Atmospheric*
 1302 *and Oceanic Technology*., 25, 1744–1754, [https://doi:](https://doi:10.1175/2008JTECHA1082.1)
 1303 <http://dx.doi.org/10.1175/2008JTECHA1082.1>.
 1304
- 1305 Matsueda, H., Machida, T., Sawa, Y., Nakagawa, Y., Hirokani, K., Ikeda, H., Kondo, N.,
 1306 & Goto, K. (2008). Evaluation of atmospheric CO₂ measurements from new flask air
 1307 sampling of JAL airliner observations. *Meteorology and Geophysics*, 59, 1-17. [https://](https://doi:10.2467/mripapers.59.1)
 1308 doi:10.2467/mripapers.59.1
 1309
- 1310 Niwa, Y., Patra, P. K., Sawa, Y., Machida, T., Matsueda, H., Belikov, D., Maki, T., Ikegami,
 1311 M., Imasu, R., Maksyutov, S., Oda, T., Satoh, M., & Takigawa, M. (2011). Three-dimensional
 1312 variations of atmospheric CO₂: aircraft measurements and multi-transport model simulations.
 1313 *Atmos. Chem. Phys.*, 11, 13359–13375. <https://doi:10.5194/acp-11-13359-2011>.
 1314
- 1315 Niwa, Y., Machida, T., Sawa, Y., Matsueda, H., Schuck, T. J., Brenninkmeijer, C. A. M.,
 1316 Imasu, R., & Satoh, M. (2012). Imposing strong constraints on tropical terrestrial CO₂
 1317 fluxes using passenger aircraft based measurements. *Journal of Geophysical. Research*,
 1318 117, D11303. <https://doi:10.1029/2012JD017474>.
 1319
- 1320 Patra, P. K., Law R. M., Peters W., Roödenbeck C., Takigawa M., Aulagnier C., Baker I.,
 1321 Bergmann, D. J., Bousquet, P., Brandt, J., Bruhwiler, L., Smith, P. J. C., Christensen, J. H.,
 1322 Delage, F., Denning, A. S., Fan, S., Geels, C., Houweling, S., Imasu, R., Karstens, U., Kawa,
 1323 S. R., Kleist, J., Krol, M. C., Lin, S.-J., Lokupitiya, R., Maki, T., Maksyutov, S., Niwa, Y.,
 1324 Onishi, R., Parazoo, N., Pieterse, G., Rivier, L., Satoh, M., Serrar, S., Taguchi, S., Vautard, R.,
 1325 Vermeulen, A. T., & Zhu Z. (2008). TransCom model simulations of hourly atmospheric CO₂:
 1326 Analysis of synoptic-scale variations for the period 2002-2003. *Global Biogeochemical Cycles*,
 1327 22, GB4013. <https://doi:10.1029/2007GB003081>
 1328

- 1329 Patra, P. K., Niwa, Y., Schuck, T. J., Brenninkmeijer, C. A. M., Machida, T., Matsueda,
 1330 H., & Sawa, Y. (2011). Carbon balance of South Asia constrained by passenger aircraft
 1331 CO₂ measurements. *Atmos. Chem. Phys.*, 11, 4163-4175. [https://doi.org/10.5194/acp-11-4163-](https://doi.org/10.5194/acp-11-4163-2011)
 1332 2011
- 1333
 1334 Patra, P. K., Canadell, J. G., Houghton, R. A., Piao, S. L., Oh, N.-H., Ciais, P., Manjunath, K.
 1335 R., Chhabra, A., Wang, T., Bhattacharya, T., Bousquet, P., Hartman, J., Ito, A., Mayorga, E.,
 1336 Niwa, Y., Raymond, P., Sarma, V. V. S. S., & Lasco, R. (2012). The carbon budget of South
 1337 Asia. *Biogeosciences Discuss.*, 9, 13537–13580. <http://doi.org/10.5194/bgd-9-13537-2012>
 1338
- 1339 Patra, P. K., Canadell, J. G., Houghton, R. A., Piao, S. L., Oh, N. –H., Ciais, P., Manjunath,
 1340 K. R., Chhabra, A., Wang, T., Bhattacharya, T., Bousquet, P., Hartman, J., Ito, A.,
 1341 Mayorga, E., Niwa, Y., Raymond, P. A., Sarma, V. V. S. S., & Lasco, R. (2013). The
 1342 carbon budget of South Asia. *Biogeosciences*, 10, 513-527. [https://doi.org/10.5194/bg-10-513-](https://doi.org/10.5194/bg-10-513-2013)
 1343 2013
- 1344
 1345 Perera, K.M.P., Lokupitiya, R.S., Zupanski, D., Denning, A.S., Meegama, R.G.N., Lokupitiya,
 1346 E.Y.K., & Patra, P.K. (2017). *Estimation of Asian and Global Carbon Fluxes Using Maximum*
 1347 *Likelihood Ensemble Filter (MLEF)*, Paper presented at International Conference on Climate
 1348 Change - 2017, Colombo, Sri Lanka.
- 1349
 1350 Peters, W., Miller, J. B., Whitaker, J., Denning, A. S., Hirsch, A., Krol, M. C., Zupanski,
 1351 D., Bruhwiler, L., & Tans, P. P. (2005). An ensemble data assimilation system to estimate
 1352 CO₂ surface fluxes from atmospheric trace gas observations. *Journal of Geophysical*
 1353 *Research*, 110, D24304. <https://doi.org/10.1029/2005JD006157>.
- 1354
 1355 Peters, W., Jacobson, A. R., Sweeney, C., Andrews, A. E., Conway, T. J., Masarie, K., Miller,
 1356 J. B., Bruhwiler, L. M. P., Pétron, G., Hirsch, A. I., Worthy, D. E. J., Werf, G. R. van der,
 1357 Randerson, J. T., Wennberg, P. O., Krol, M. C., & Tans, P. P. (2007). An atmospheric
 1358 perspective on North American carbon dioxide exchange: CarbonTracker. *PNAS*, 104, 18925-
 1359 18930. <https://www.pnas.org/content/pnas/104/48/18925.full.pdf>
 1360
- 1361 Peylin, P., Law, R. M., Gurney, K. R., Chevallier, F., Jacobson, A. R., Maki, T., Niwa, Y.,
 1362 Patra P. K., Peters, W., Rayner, P. J., Rödenbeck, C., van der Laan-Luijkx, I. T., & Zhang,
 1363 X. (2013). Global atmospheric carbon budget: results from an ensemble of atmospheric
 1364 CO₂ inversions. *Biogeosciences*, 10, 6699–6720. <https://doi.org/10.5194/bg-10-6699-2013>
 1365
- 1366 Piao, S., Fang, J., Ciais, P., Peylin, P., Huang, Y., Sitch, S., & Wang, T. (2009). The carbon
 1367 balance of terrestrial ecosystems in China. *Nature*, 458, 1009-1013. [https://doi:](https://doi.org/10.1038/nature07944)
 1368 10.1038/nature07944
- 1369
 1370 Piao, S. L., Ito, A., Huang, S. G. Li, Y., Ciais, P., Wang, X. H., Peng, S. S., Nan, H. J.,
 1371 Zhao, C., Ahlström, A., Andres, R. J., Chevallier, F., Fang, J. Y., Hartmann, J.,
 1372 Huntingford, C., Jeong, S., Levis, S., Levy, P. E., Li, J. S., Lomas, M. R., Mao, J. F.,
 1373 Mayorga, E., Mohammat, A., Muraoka, H., Peng, C. H., Peylin, P., Poulter, B., Shen, Z.
 1374 H., Shi, X., Sitch, S., Tao, S., Tian, H. Q., Wu, X. P., Xu, M., Yu, G. R., Viovy, N., Zaehle,
 1375 S., Zeng, N., & Zhu, B. (2012). The carbon budget of terrestrial ecosystems in East Asia
 1376 over the last two decades. *Biogeosciences*, 9, 3571–3586. [https://doi.org/10.5194/bg-9-3571-](https://doi.org/10.5194/bg-9-3571-2012)
 1377 2012
- 1378

- 1379 Ro^odenbeck, C., Houweling, S., Gloor, M., & Heimann, M. (2003). CO₂ flux history 1982–
 1380 2001 inferred from atmospheric data using a global inversion of atmospheric transport.
 1381 *Atmos. Chem. Phys.*, 3, 1919–1964. <https://doi.org/10.5194/acp-3-1919-2003>
 1382
- 1383 Saeki, T., Maksyutov, S., Saito, M., Valsala, V., Oda, T., Andres, R. J., Belikov, D., Tans, P.,
 1384 Dlugokencky, E., Yoshida, Y., Morino, I., Uchino, O., & Yokota, T. (2013). Inverse Modeling
 1385 of CO₂ Fluxes Using GOSAT Data and Multi-Year Ground-Based Observations. *SOLA*, 9,
 1386 45–50. <https://doi:10.2151/sola.2013-011>
 1387
- 1388 Sajeev, P., Johnson, M. S., Potter, C., Genovesse, V., Baker, D. F., Haynes, K. D., Henze, D.
 1389 K., Liu J., & Poulter, B. (2019). Prior biosphere model impact on global terrestrial CO₂ fluxes
 1390 estimated from OCO-2 retrievals. *Atmos. Chem. Phys.*, 19, 13267–13287.
 1391 <https://doi.org/10.5194/acp-19-13267-2019>
 1392
- 1393 Sawa, Y., Machida, T., & Matsueda, H. (2012). Aircraft observation of the seasonal variation
 1394 in the transport of CO₂ in the upper atmosphere. *Journal of Geophysical Research*, 117,
 1395 D05305. <https://doi:10.1029/2011JD016933>.
 1396
- 1397 Schuh, A. E., Denning, A. S., Corbin, K. D., Baker, I. T., Uliasz, M., Parazoo, N., Andrews,
 1398 A. E., & Worthy, D. E. J. (2010). A regional high-resolution carbon flux inversion of North
 1399 America for 2004. *Biogeosciences*, 7, 1625–1644, <https://doi:10.5194/bg-7-1625-2010>
 1400
- 1401 Tans, P. P., Fung, I. Y., & Takahashi, T. (1990). Observational constraints on the global
 1402 atmospheric CO₂ budget. *Science*, 247, 1431–1438. [http://links.jstor.org/sici?sici=0036-
 1403 8075%2819900323%293%3A247%3A4949%3C1431%3AOCOTGA%3E2.0.CO%3B2-N](http://links.jstor.org/sici?sici=0036-8075%2819900323%293%3A247%3A4949%3C1431%3AOCOTGA%3E2.0.CO%3B2-N)
 1404
- 1405 Thompson, R.L., Patra, P.K., Chevallier, F., Maksyutov, S., Law, R.M., Ziehn, T., Luijkx,
 1406 I.T. van der Laan, Peters, W., Ganshin, A., Zhuravlev, R., Maki, T., Nakamura, T., Shirai,
 1407 T., Ishizawa, M., Saeki, T., Machida, T., Poulter, B., Canadell, J. G. & Ciais, P. (2016).
 1408 Top-down assessment of the Asian carbon budget since the mid 1990s. *Nature*
 1409 *Communications*, 7:10724. <https://doi:10.1038/ncomms10724>
 1410
- 1411 Takahashi, T., Sutherland, S. C., Sweeney, C., Poisson, A., Metzl, N., Tilbrook, B., Bates,
 1412 N., Wanninkhof, R., Feely, R. A., Sabine, C., Olafsson, J., & Nojiri, Y. (2002). Global
 1413 sea-air CO₂ flux based on climatological surface ocean pCO₂, and seasonal biological and
 1414 temperature effects. *Deep-Sea Res. Part II*, 49, 1601–1622. [https://doi:10.1016/S0967-
 1415 0645\(02\)00003-6](https://doi:10.1016/S0967-0645(02)00003-6)
 1416
- 1417 Whitaker, J. S., & Hamill, T. M., (2002). Ensemble Data Assimilation without Perturbed
 1418 Observations. *Monthly Weather Review*, 130 (7), 1913–1924. [https://doi.org/10.1175/1520-
 1419 0493\(2002\)130<1913:EDAWPO>2.0.CO;2](https://doi.org/10.1175/1520-0493(2002)130<1913:EDAWPO>2.0.CO;2)
 1420
- 1421 Zhang, H. F., Chen, B. Z., Luijkx, I. T. van der L., Machida, T., Matsueda, H., Sawa, Y.,
 1422 Fukuyama, Y., Langenfelds, R., Schoot M. van der, Xu, G., Yan, J. W., Cheng, M. L.,
 1423 Zhou, L. X., Tans, P. P., & Peters W. (2014). Estimating Asian terrestrial carbon fluxes
 1424 from CONTRAIL aircraft and surface CO₂ observations for the period 2006–2010. *Atoms.*
 1425 *Chem. Phys.*, 14, 5807–5824. <https://doi:10.5194/acp-14-5807-2014>
 1426
- 1427 Zupanski, M. (2005). Maximum likelihood ensemble filter: Theoretical aspects. *Monthly*
 1428 *Weather Review*, 133(6), 1710–1726. <https://doi.org/10.1175/MWR2946.1>

1429 Zupanski, D., Denning, A. S., Uliasz, M., Zupanski, M., Schuh, A. E., Rayner, P. J., &
 1430 Peters, W. (2007). Carbon flux bias estimation employing Maximum Likelihood Ensemble
 1431 Filter (MLEF). *Journal of Geophysical Research*, 112, D17107. [https://](https://doi:10.1029/2006JD008371)
 1432 doi:10.1029/2006JD008371.

1433

1434

1435

1436 **Figure 1.** A map of the continuous and flask stations used in this study except CONTRAIL.
 1437 Open circles depict continuous measurement sites (see Table 1). Crosses identify flask-
 1438 sampling locations that are part of the NOAA-ESRL network (GLOBALVIEW-CO2).

1439

1440 **Figure 2.** Variation of the observation errors for Continuous stations for the years 2009-2011.

1441

1442 **Figure 3.** Variation of the observation errors for Flask stations for the years 2009-2011.

1443

1444 **Figure 4.** Variation of the observation errors for CONTRAIL locations for the years 2009-
 1445 2011.

1446

1447 **Figure 5.** Observed hourly CO₂ concentrations (in blue) and simulated CO₂ (in red) from
 1448 PCTM for years from 2009 – 2011 at stations FSD (Fraserdale, Canada), AMT (Argyle, Maine,
 1449 United States) and BRW (Barrow Atmospheric Baseline Observatory, United States).

1450

1451 **Figure 6.** Daily time series plots of CO₂ concentrations from posterior fluxes (in red) and prior
 1452 fluxes (in black) compared to observations (in blue) for years 2009 – 2011 at Yonagunijima,
 1453 Japan (YON), Ryori, Japan (RYO), Anmyeon-do, Republic of Korea (AMY), Argyle, Maine,
 1454 United States (AMT), Chibougamau, Canada (CHM) and Anmyeon-do, Republic of Korea
 1455 (AMY)

1456

1457 **Figure 7.** Variation of CONTRAIL CO₂ observations with relevant altitude (m).

1458

1459 **Figure 8.** Distribution of the difference between observed CO₂ and recovered CO₂ under four
 1460 vertical bins for years 2009 to 2011.

1461

1462 **Figure 9.** Stations map with CONTRAIL locations and mean annual percentage uncertainty
 1463 reduction for the years (a) 2009, (b) 2010 and (c) 2011.

1464

1465 **Figure 10.** Stations map for MLEF (Left panel) and CT2017 (Right panel)

1466

1467 **Figure 11.** Recovered Mean Annual NEE by MLEF (Left panel) and CT (CT2017) (Right
 1468 panel) for the year (a) 2009, (b) 2010 and (c) 2011 respectively. Units: gC m⁻² yr⁻¹.

1469

1470 **Figure 12.** Mean annual NEE with 1-σ error bars aggregated to TransCom regions; Boreal
 1471 North America, Temperate North America, Europe, Tropical Asia, Eurasian Temperate and
 1472 Australia, estimated by MLEF and CarbonTracker (a) for 2009, (b) for 2010 and (c) for 2011.
 1473 Units: GtC/year.

1474

1475 **Figure 13.** Comparison of optimized surface CO₂ fluxes (GtC yr⁻¹) from MLEF with other
 1476 studies

1477 ^aBiomass burning emissions are included into the land fluxes

1478 **Table 1.** Continuous and Flask CO₂ measurement sites used in this study

1479 **Table 2.** Root Mean Square Error (RMSE) with respect to the prior and the posterior at
1480 continuous sites for 2009 to 2011 Units: parts per million by volume (ppmv)

1481 **Table 3.** Root Mean Square Error (RMSE) with respect to the posterior CONTRAIL CO₂
1482 measurements for 2009 to 2011 Units: parts per million by volume (ppmv)

1483 **Table 4.** Optimized surface CO₂ fluxes and their one-sigma uncertainties (PgCyr⁻¹) for the
1484 selected TransCom regions from 2009 to 2011 using MLEF and CT2017 method